Dynamic parameter estimation of atomic layer deposition kinetics applied to in situ quartz crystal microbalance diagnostics

Holmqvist, Anders; Törndahl, Tobias; Magnusson, Fredrik; Zimmermann, Uwe; Stenström, Stig

Published in:
Chemical Engineering Science

DOI:
10.1016/j.ces.2014.02.005

2014

Document Version:
Peer reviewed version (aka post-print)

Dynamic Parameter Estimation of Atomic Layer Deposition Kinetics Applied to *in situ* Quartz Crystal Microbalance Diagnostics

A. Holmqvist[a,*], T. Törndahl[b], F. Magnusson[c], U. Zimmermann[b], S. Stenström[a]

[a] *Department of Chemical Engineering, Lund University, P.O. Box 124, SE-221 00 Lund, Sweden*
[b] *Ångström Solar Center, Solid State Electronics, Uppsala University, P.O. Box 534, SE-751 21 Uppsala, Sweden*
[c] *Department of Automatic Control, Lund University, P.O. Box 118, SE-221 00 Lund, Sweden*

Abstract

This paper presents the elaboration of an experimentally validated model of a continuous cross-flow atomic layer deposition (ALD) reactor with temporally separated precursor pulsing encoded in the Modelica language. For the experimental validation of the model, *in situ* quartz crystal microbalance (QCM) diagnostics was used to yield submonolayer resolution of mass deposition resulting from thin film growth of ZnO from $Zn(C_2H_5)_2$ and H_2O precursors. The ZnO ALD reaction intrinsic kinetic mechanism that was developed accounted for the temporal evolution of the equilibrium fractional surface concentrations of precursor adducts and their transition states for each half-reaction. This mechanism was incorporated into a rigorous model of reactor transport, which comprises isothermal compressible equations for the conservation of mass, momentum and gas-phase species. The physically based model in this way relates the local partial pressures of precursors to the dynamic composition of the growth surface, and ultimately governs the accumulated mass trajectory

*Corresponding author. Tel.: +46 46 222 8301; fax: +46 46 222 4526
Email addresses: anders.holmqvist@chemeng.lth.se (A. Holmqvist), tobias.torndahl@angstrom.uu.se (T. Törndahl), fredrik.magnusson@control.lth.se (F. Magnusson), uwe.zimmermann@angstrom.uu.se (U. Zimmermann), stig.stenstrom@chemeng.lth.se (S. Stenström)

at the QCM sensor. Quantitative rate information can then be extracted by means of dynamic parameter estimation. The continuous operation of the reactor is described by limit-cycle dynamic solutions and numerically computed using Radau collocation schemes and solved using CasADi's interface to IPOPT. Model predictions of the transient mass gain per unit area of exposed surface QCM sensor, resolved at a single pulse sequence, were in good agreement with experimental data under a wide range of operating conditions. An important property of the limit-cycle solution procedure is that it enables the systematic approach to analyze the dynamic nature of the growth surface composition as a function of process operating parameters. Especially, the dependency of the film growth rate per limit-cycle on the half-cycle precursor exposure dose and the process temperature was thoroughly assessed and the difference between ALD in saturating and in non-saturating film growth conditions distinguished.
Keywords: Atomic layer deposition, Mathematical modeling, *in situ* film characterization, Experimental model validation, Parameter identification, Optimization

1. Introduction

Atomic layer deposition (ALD) is a gas-phase deposition process capable of producing conformal thin films with controlled uniform thickness in the nanometer range (George, 2010). Conventional thermal ALD is a special modification of the chemical vapor deposition (CVD) technique and relies on decoupling self-terminating (Puurunen, 2005b) gas–surface reactions (Masel, 1996). Precursors are injected in a non-overlapping alternate manner, separated by intermediate purge steps, and this prevents reaction in the gas-phase (Miikkulainen et al., 2013).

Industrial semiconductor processing has been a major stimulant for the development of the ALD process (Ritala and Niinisto, 2009; Sneh et al., 2002). Novel applications of ALD are expanding beyond semiconductor processing in several emerging areas, such as surface passivation layers in c-Si solar cells, buffer

layers in $CuIn_{1-x}Ga_xSe_2$ (CIGS) solar cells (Bakke et al., 2011), and diffusion barrier layers in OLEDs and thin-film photovoltaics (Carcia et al., 2009). High-throughput and low cost ALD production techniques are consequently becoming ever-more necessary (Poodt et al., 2012). In this context, Wolden et al. (2011) have pointed out that the development of comparative manufacturing techniques requires sophisticated modeling to understand how to maintain cross-substrate film thickness uniformity (Cleveland et al., 2012; Henn-Lecordier et al., 2011).

The development of validated, predictive physical ALD process models is limited by a lack of reliable values for the parameters of the physicochemical phenomena that govern the ALD film growth. Thus, the calibration and experimental validation of models have been identified as an essential step in the field (Semiconductor Industry Association, 2011). There are two generic methodologies for development of ALD reaction intrinsic kinetic mechanisms in the literature:

i) Methods based on *ab initio* quantum chemistry, in which the energy parameters of the relevant gas–surface reactions are estimated using calculations based on density functions, and the associated rate parameters, using Rice–Ramsperger–Kassel–Marcus theory (Deminsky et al., 2004; Travis and Adomaitis, 2013a,b). Elliott (2012) gives an overview of primary studies of ALD via atomic-scale simulation.

ii) Methods based on statistical model calibration and experimental validation, in which the kinetic parameters are obtained from *ex situ* experimental film characterization that elucidates ALD chemistry (Holmqvist et al., 2013a; Lim et al., 2000; Park et al., 2000).

The ITRS, however, has suggested that *in situ* monitoring technologies, including transmission Fourier transform infrared spectroscopy (Dillon et al., 1995; Ferguson et al., 2000), quartz crystal microbalance (QCM) (Aarik et al., 1994a,b, 2001; Fan and Toyoda, 1992) and quadrupole mass spectroscopy (Juppo et al., 2000; Lei et al., 2006; Rahtu and Ritala, 2002b), should be used to analyze highly non-equilibrium ALD processes, in order to increase the accuracy of

the model calibration (Semiconductor Industry Association, 2011). These techniques provide extensive real-time information of the process chemistry and reactor conditions.

The overall objective of this study was to develop a general method to calibrate the parameters of reduced ALD reaction intrinsic kinetic mechanisms, including only the principal sequential and parallel elementary surface reactions, using *in situ* QCM diagnostics. This methodology developed was subsequently applied to a case study in which thin ZnO films were deposited from $Zn(C_2H_5)_2$ and H_2O precursors. This paper focuses around three main points:

i) To investigate experimentally transient film growth in the continuous cross-flow ALD reactor system F-120 manufactured by ASM Microchemistry Ltd. (Suntola, 1992) with *in situ* QCM diagnostics.

ii) To develop a physically based model of continuous cross-flow, low-volume ALD reactors with temporal precursor pulsing, and to incorporate ALD surface reaction intrinsic kinetics.

iii) To formulate and solve a dynamic non-convex parameter estimation problem using measurements from the *in situ* QCM, and to assess the reliabilities of the parameter estimates and the predicted model responses.

This paper is organized as follows. Section 2 presents the continuous cross-flow ALD reactor system and the experimental investigation. Section 3 outlines the ALD reaction intrinsic kinetic mechanism. Section 4 is dedicated to the development of the ALD reactor model. Section 5 describes the formulation of the dynamic non-convex parameter estimation problem, while Section 6 outlines the modeling and optimization environment. Section 7 presents the primary results from the statistical model calibration and experimental validation, and Section 8 contains concluding remarks.

2. Reactor System Setup and Experimental Investigation

2.1. Process Description

The continuous cross-flow ALD reactor system F-120 (Fig. 1a) manufactured by ASM Microchemistry Ltd. (Suntola, 1992) was used for the controlled deposition of thin ZnO films from $Zn(C_2H_5)_2$ and H_2O precursors. Briefly, the reactor setup incorporates actuator subsystems that provide flow control (FC) of the carrier gas and each precursor inflow, $\dot{Q}_\alpha$ and $\alpha \in \{N_2, Zn(C_2H_5)_2, H_2O\}$, and that enable alternate injections with variable dose times, Δt_α, of the αth precursor. The normalized boxcar function, $\Pi_\alpha(t, \Delta t_\alpha) \in [0, 1]$, was used to model non-overlapping precursor injections in a cyclic time sequence, where this function is:

$$\Pi_\alpha(t, \Delta t_\alpha) = \begin{cases} 1 & \gamma_\alpha \sum\limits_{\beta \neq \alpha} \Delta t_\beta \leq \bar{t} \leq \gamma_\alpha \sum\limits_{\beta \neq \alpha} \Delta t_\beta + \Delta t_\alpha \\ 0 & \text{otherwise} \end{cases} \tag{1}$$

in which $\bar{t} = (N_{\Delta t} - \lfloor N_{\Delta t} \rfloor)\Delta t$ is the normalized cycle time, $N_{\Delta t} = t(\Delta t)^{-1}$ is the cycle number, $\Delta t = \Delta t_{Zn(C_2H_5)_2} + \Delta t_{N_2} + \Delta t_{H_2O} + \Delta t_{N_2}$ denotes one complete ALD cycle, and $[\gamma_{Zn(C_2H_5)_2}, \gamma_{H_2O}] = [0, 1]$.

The continuous inert gas flow, $\dot{Q}_{N_2}$,transports traveling waves of adsorptive precursors laterally across the substrate holders, which are mounted on opposite sides of the reaction chamber (RC), see Fig. 1b. The equipment has been redesigned such that a wall-mounted quartz crystal resonator can be mounted horizontally inside the chamber at the level of the surface of the custom-built substrate holder, thereby avoiding any perturbation of the hydrodynamic flow field (Riha et al., 2012; Yousfi et al., 2000). The rear of the crystal is exposed to a higher partial pressure of N_2 to prevent back-side deposition (Elam et al., 2002).

The reaction chamber and the precursor forelines are placed into a quartz glass tube of length 1.20 (m), divided into five independently heated zones. The temperature, T, is controlled by external induction heating that provides the desired temperature profile. The temperature control (TC) equipment comprises

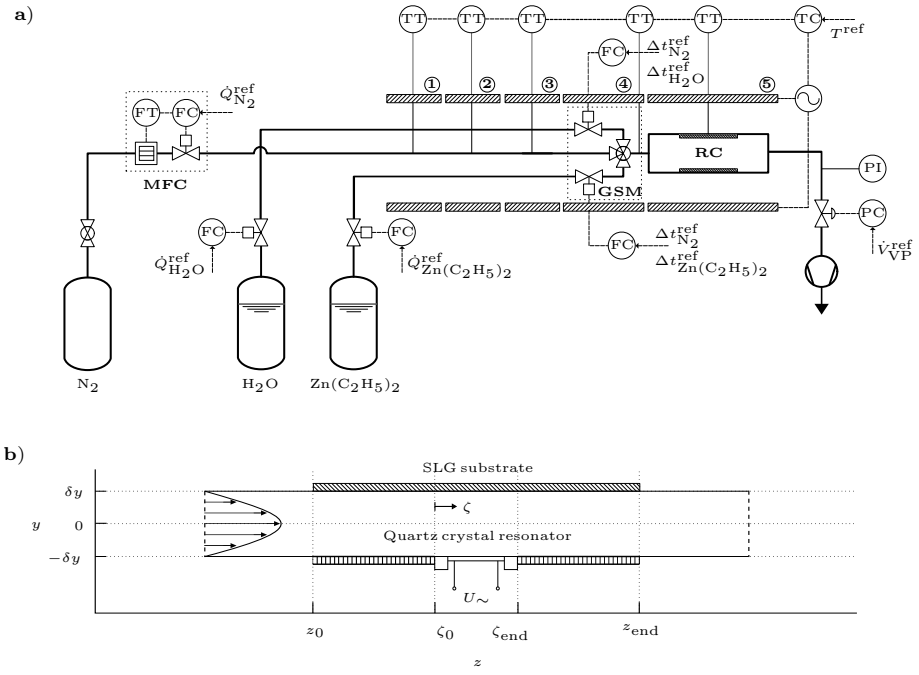

Figure 1: a) Simplified P&ID of the continuous cross-flow ALD reactor system F120 by ASM Microchemistry Ltd. (Suntola, 1992). It is noteworthy that the three-way gas switching mechanism (GSM) is an inherent physical structure of the RC inlet (see, e.g. Baunemann (2006)). b) Representation of the reaction chamber showing the wall-mounted quartz crystal resonator. The soda lime glass (SLG) substrate dimension is $z_{\mathrm{end}} - z_0 = 5.0$ (cm) and the exposed quartz crystal dimension is $\zeta_{\mathrm{end}} - \zeta_0 = 0.9$ (cm).

chromel-alumel thermocouples attached to the outside of the flow tube under the heaters, maintained by PID controllers. Finally, the pressure, p, at the reaction chamber outlet (subject to the total $\mathrm{N_2}$ mass flow and temperature) is maintained by pressure control (PC) equipment that comprises a rotary vane vacuum pump (VP) operating at constant flow, $\dot{V}_{\mathrm{VP}}$. The vector of manipulated variables is thus $\mathbf{u} = [\, T, \dot{V}_{\mathrm{VP}}, \dot{Q}_{\mathrm{N_2}}, \Delta t_{\mathrm{N_2}}, \dot{Q}_{\mathrm{Zn(C_2H_5)_2}}, \Delta t_{\mathrm{Zn(C_2H_5)_2}}, \dot{Q}_{\mathrm{H_2O}}, \Delta t_{\mathrm{H_2O}}]^T$.

2.2. Instrumentation and Data Acquisition

QCM measurements were obtained using a commercial Inficon SQM-160 thin film deposition monitor, from which the period of the QCM crystal was recorded by a personal computer at 10.0 (Hz). The quartz crystals were AT-cut, had a diameter of 1.9 (cm), and operated at a nominal frequency of 6.0 (MHz) in the fundamental mode. A detailed description of the QCM used to monitor ALD in viscous flow reactor designs has been previously presented: see, e.g., Elam et al. (2002). Assuming that the acoustic impedance of the deposited film is equal to the acoustic impedance of an AT-cut crystal (Dunham et al., 1995), the relationship between the change of resonant frequency, $\Delta\hat{f}_q$, and the incremental change in mass, $\Delta\hat{m}_q$, can be obtained from the Sauerbrey equation (Sauerbrey, 1959):

$$\Delta\hat{f}_q = -\frac{2\hat{f}_{0,q}^2}{A_q(\mu_q\rho_q)^{\frac{1}{2}}}\Delta\hat{m}_q \tag{2}$$

in which $f_{0,q}$ is the fundamental resonant frequency, A_q the exposed surface area, ρ_q the density of the quartz crystal, and μ_q its shear modulus. However, Eq. (2) must be extended for heavily loaded crystals to incorporate the acousto-elastic properties of the deposit (Lu and Lewis, 1972; Wajid, 1991).

In addition, reference values of the total mass gain per cycle (MGPC) (Wind and George, 2010) were obtained from *ex situ* measurements conducted using X-ray reflectivity (XRR) with a Philips X'pert MRD powder diffractometer equipped with a slit system, see e.g. Holmqvist et al. (2012); Törndahl et al. (2007) for detailed descriptions. These measurements were taken at the central sampling position on the SLG substrate (see Fig. 1b) after $N_{\Delta t} = 2.5 \cdot 10^2$ (cycles), and were used to calibrate the MGPC, $d\Delta\hat{m}_q|_{\Delta t}(dN_{\Delta t})^{-1}$, extracted from the film mass increment trajectories, $\Delta\hat{m}_q$. Table 1 lists MGPC values obtained from experimental QCM and XRR measurements.

2.3. Minimization of Temperature-induced Apparent QCM Mass Transients

The QCM is extremely useful for probing the ALD surface reactions because of its submonolayer resolution and rapid time response. However, the

Table 1: Outline of the experimental design. The determined mass gain per cycle, $d\Delta\hat{m}_q|_{\Delta t}(dN_{\Delta t})^{-1}$, and the average number of hydroxyl groups that reacted with each $Zn(C_2H_5)_2$ molecule, $\hat{\nu}$, are listed for each experimental index, j. All experiments were performed with the following process operating parameters: $[\dot{Q}_{Zn(C_2H_5)_2}, \dot{Q}_{H_2O}, \dot{Q}_{N_2}] = [8.9, 3.7, 500.0]$ (sccm) [standard cubic centimeters per minute at STP]. It is noteworthy that the real pulse duration, Δt_α, is approximately equal to $1.12 \cdot \widetilde{\Delta t}$ and that $\forall\alpha \in \{N_2, Zn(C_2H_5)_2, H_2O\}$. The density, ρ_s, of the ZnO film deposited at $T = 150$ (°C) was 5.4 (g cm^{-3}) when analyzed with XRR (Törndahl et al., 2007).

j	$\widetilde{\Delta t}_{Zn(C_2H_5)_2}$ (s)	$\widetilde{\Delta t}_{H_2O}$ (s)	$\widetilde{\Delta t}_{N_2}$ (s)	T (°C)	$\frac{d\Delta\hat{m}_q\|_{\Delta t}}{dN_{\Delta t}}$ (Å cycle^{-1})	$\hat{\nu}$ (a.u.)
1	0.4	0.4	0.8	100	0.55 ± 0.031	1.25 ± 0.172
2	0.4	0.4	2.0	100	0.56 ± 0.034	1.33 ± 0.210
3	1.0	1.0	2.0	100	1.12 ± 0.037	1.30 ± 0.118
4[a]	2.0	2.0	2.0	100	1.62 ± 0.056	1.28 ± 0.084
5	0.4	0.4	0.8	125	1.32 ± 0.041	1.38 ± 0.079
6	0.4	0.4	2.0	125	1.30 ± 0.023	1.39 ± 0.059
7[a]	1.0	1.0	2.0	125	1.77 ± 0.060	1.44 ± 0.066
8	2.0	2.0	2.0	125	1.97 ± 0.069	1.39 ± 0.076
9	0.4	0.4	0.8	150	1.66 ± 0.081	1.34 ± 0.082
10	0.4	0.4	2.0	150	1.63 ± 0.048	1.41 ± 0.067
11	1.0	1.0	2.0	150	1.94 ± 0.082	1.30 ± 0.102
12	2.0	2.0	2.0	150	2.05 ± 0.070	1.33 ± 0.084
13[a]	0.4	0.4	0.8	175	1.80 ± 0.061	1.34 ± 0.101
14	0.4	0.4	2.0	175	1.78 ± 0.036	1.44 ± 0.064
15	1.0	1.0	2.0	175	2.00 ± 0.058	1.31 ± 0.106
16	2.0	2.0	2.0	175	2.06 ± 0.057	1.35 ± 0.150
17	0.4	0.4	0.8	200	1.80 ± 0.050	1.40 ± 0.129
18	0.4	0.4	2.0	200	1.76 ± 0.038	1.38 ± 0.053
19	1.0	1.0	2.0	200	1.98 ± 0.054	1.33 ± 0.109
20	2.0	2.0	2.0	200	2.04 ± 0.066	1.35 ± 0.070
i[b]	0.4	0.4	0.8	100	0.55	
ii[b]	0.4	0.4	0.8	125	1.32	
iii[b]	0.4	0.4	0.8	150	1.66	
iv[b]	0.4	0.4	0.8	175	1.80	
v[b]	0.4	0.4	0.8	200	1.80	

[a]Experimental validation set.

[b]*Ex situ* XRR references set with $N_{\Delta t} = 2.5 \cdot 10^2$ (cycles).

most serious limitation to the QCM technique is that the resonant frequency of the AT-cut quartz crystal is dependent on temperature (Elam et al., 2002; Elam and Pellin, 2005). Consequently, fluctuations in temperature lead to large fluctuations in apparent mass. Rocklein and George (2003) demonstrated that temperature transients caused by gas pulsing can be minimized by tuning the temperature profile along the zones that lie upstream of the reaction chamber. Many studies have subsequently shown that nearly ideal ALD growth that behaves according to the expectations from the ALD surface chemistry can be successfully monitored once the temperature profile has been optimized to minimize the temperature-induced apparent mass changes (see, e.g. Larrabee et al. (2013); Riha et al. (2012) and the reference cited therein).

In this study, the temperature profile prescribed by the four individually heated zones upstream of the RC (see Fig. 1) was tuned for each deposition temperature studied (see Table 1) in order to minimize the temperature-induced mass changes when a fully hydroxylated QCM sensor was exclusively exposed to the H_2O precursor. Hence, no ALD growth is expected to occur in these conditions and the apparent mass change was a result of temperature fluctuations. Furthermore, baseline subtraction of the temperature-induced drift (Rahtu and Ritala, 2002a) was not considered necessary.

2.4. Experimental Investigation

The experimental design was intended to assess the impact of Δt_α, $\alpha \in \{N_2, Zn(C_2H_5)_2, H_2O\}$, and the RC temperature, T, on the rate at which the film was deposited. Furthermore, the design ensured that the experiments gave the maximum possible information, in a statistical sense, which maximized the capacity to discriminate between calibration parameters (Franceschini and Macchietto, 2008). The ALD reactor was operated in a wide range of process conditions in order to understand the complex interdependence between the sequential and parallel elementary surface reactions. This complexity arises in that the reactivity in one half-cycle is influenced by that in the half-cycle that precedes it (Kuse et al., 2003; Ritala and Leskelä, 2002). The examined range of process

conditions defines the region of validity of the model and includes the bounds of the ALD window (Yousfi et al., 2000) for both saturated and non-saturated (Park et al., 2000) deposition. The dose times for $Zn(C_2H_5)_2$ and H_2O were varied between $\widetilde{\Delta t}_\alpha \in [0.4, 2.0]$ (s), with purge times in the range $\widetilde{\Delta t}_\beta \in [0.8, 2.0]$ (s) between precursor pulses (see Table 1). The N_2 purge times were intentionally longer than necessary to separate the QCM signals that resulted from the individual precursor exposures (Jur and Parsons, 2011). Rocklein and George (2003) have shown also that long purge times decrease the QCM error.

In this study, datasets of $N_{\Delta t} \geq 50$ (cycles) were collected for each experimental case, j, and the average mass increment trajectory, $\langle \Delta \hat{m}_q \rangle$, was used for experimental validation, see Fig. 2. The rate of deposition deviated from constant MGPC, $d^2 \Delta \hat{m}_q|_{\Delta t} (dN_{\Delta t}^2)^{-1} \neq 0$, during the first $N_{\Delta t} \leq 25$ (cycles) for every combination $j \in \{1, 2, \cdots, N_j\}$ of dose times. These changes have been attributed to the terminal coverage of active surface sites (Holmqvist et al., 2012) from the previous experimental case, j, and their extent is ultimately determined by the precursor dose times. Thus, we considered that the data collected from the $N_{\Delta t} > 25$ (cycles) of growth did not suffer from this complication, and used this data to determine $\langle \Delta \hat{m}_q \rangle$ and the associated deviation, $\hat{\sigma}_{\langle \Delta \hat{m}_q \rangle}$. Furthermore, the average number of hydroxyl groups that reacted with each $Zn(C_2H_5)_2$ molecule, $\hat{\nu}$, was determined from the ratio of mass change that occurred during the half-reactions (Elam and George, 2003) (see Table 1). The QCM mass ratio for ZnO ALD is given by:

$$\frac{\widehat{\Delta M}_B}{\widehat{\Delta M}_A} = \frac{M_{H_2O} - (2 - \hat{\nu}) M_{C_2H_6}}{M_{Zn(C_2H_5)_2} - \hat{\nu} M_{C_2H_6}} \tag{3}$$

in which the quotients of the differences in molecular masses of the outermost surface species, i.e. $\widehat{\Delta M}_B (\widehat{\Delta M}_A)^{-1}$, were extracted from the QCM trajectories (see Fig. 2). The temperature averaged mean value of the number of reacting hydroxyl groups was determined to $\langle \hat{\nu} \rangle = 1.361 \pm 0.030$, based on the mean values of $\hat{\nu}$ at each temperature in the range $T \in [100, 200]$ (°C). This value can be compared with that determined by Elam and George (2003), $\nu = 1.37$ at $T = 177$ (°C). In addition, the full monolayer-limiting molar

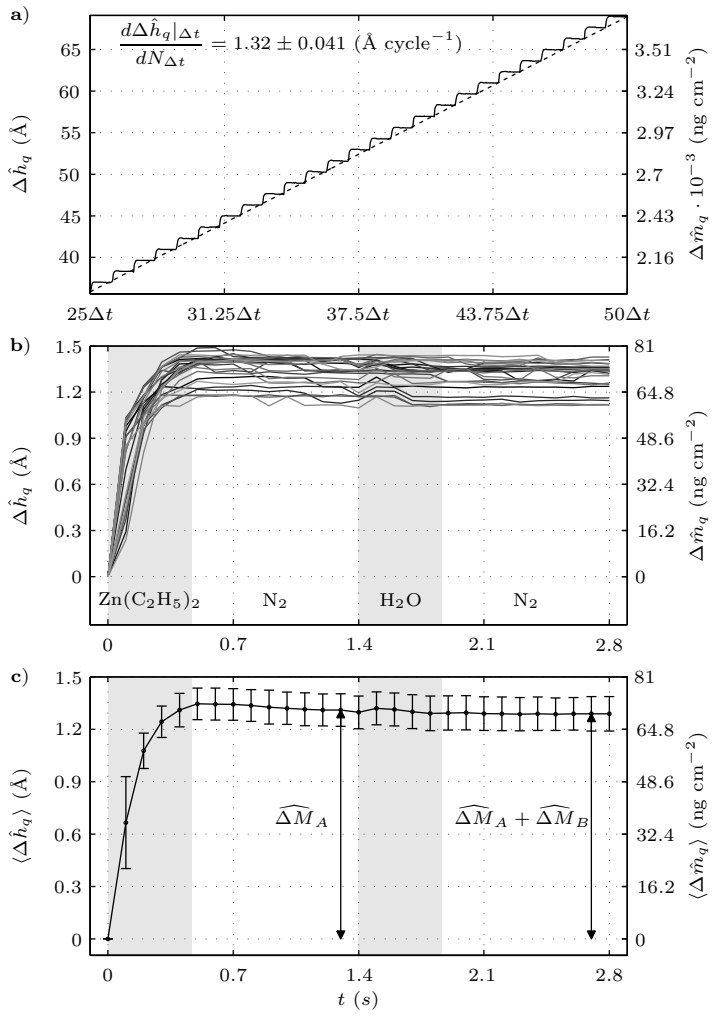

Figure 2: a) Apparent mass trajectory, $\Delta\hat{m}_q$, as a function of time for the experimental index $j = 5$ (Table 1 gives the process operating conditions). MGPCs, $d\Delta\hat{m}_q|_{\Delta t}(dN_{\Delta t})^{-1}$, have been calibrated using reference *ex situ* XRR thickness measurements. b) Fractionation of the apparent mass trajectory into individual ALD cycles, $t \in [0, \Delta t]$ (s). The shaded rectangles indicate the precursor pulse interval endpoints. c) Estimated mean mass gain, $\langle\Delta\hat{m}_q\rangle$, and associated confidence intervals, $\sigma_{\langle\Delta\hat{m}_q\rangle}$, from the individual ALD cycles.

concentration of surface sites, Λ_{ML}, can be deduced from the density of the ZnO film $\rho_{\mathrm{s}} = 5.4 \cdot 10^3\,(\mathrm{kg\,m^{-3}})$ (Törndahl et al., 2007), using the definition

$\Lambda_{\mathrm{ML}} = \left(\rho_{\mathrm{s}} M_{\mathrm{s}}^{-1} \tilde{N}\right)^{2/3} \tilde{N}^{-1} = 1.94 \cdot 10^{-5}$ $(\mathrm{mol\,m^{-2}})$, which corresponds to a film monolayer thickness $h_{\mathrm{ML}} = 2.93$ $(\mathrm{\AA\,cycle^{-1}})$. Full theoretical monolayer growth is normally not reached, however, and steric hindrance determines when saturation occurs, at which the ligand packing is at its real maximum (Puurunen, 2003). Travis and Adomaitis (2013b) have recently used the ligand group concentration at the close-packing limit experimentally determined by Puurunen (2005a) to compute the limiting surface concentrations associated with saturating ALD growth per cycle. Corresponding data are not available for the precursors used in the present study, and the limiting molar concentration of surface sites, $\Lambda = 1.37 \cdot 10^{-5}$ $(\mathrm{mol\,m^{-2}})$, was instead determined from the maximum growth per cycle, $\max d\Delta\hat{m}_q|_{\Delta t}(dN_{\Delta t})^{-1}$, (see Table 1). Finally, it is noteworthy that only this quasi-steady state growth regime is considered in this experimental investigation and, consequently, elementary surface reactions of the initial regime (Alam and Green, 2003; Puurunen, 2004), in which $d^2\Delta\hat{m}_q|_{\Delta t}(dN_{\Delta t}^2)^{-1} \neq 0$, were excluded.

3. ALD Reaction Intrinsic Kinetic Mechanism

It was assumed that both the $Zn(C_2H_5)_2$ and the H_2O half-reactions proceed through the trapping-mediated mechanism, analogous to that proposed by Ren (2009):

$$\text{reactants} \underset{\text{des}}{\overset{\text{ads}}{\rightleftharpoons}} [\text{adsorbed adduct state}] \underset{\text{rev}}{\overset{\text{fwd}}{\rightleftharpoons}} [\text{transition state}]^{\ddagger} \xrightarrow{\text{fwd}} \text{desorption state} \tag{R1}$$

where the reactions under consideration proceed through stable intermediate transition complexes formed by the species in the gas-phase reacting with an active surface site through a typical donor–acceptor coordination bond (Deminsky et al., 2004; Musgrave, 2012; Travis and Adomaitis, 2013b). The elementary gas–surface reaction mechanisms for the $Zn(C_2H_5)_2$ precursor and a normally

hydroxylated surface are thus:

$$(-\mathrm{OH})_\nu\langle \mathrm{s}\rangle + \mathrm{Zn(C_2H_5)_2}\langle \mathrm{g}\rangle \overset{i=1}{\rightleftharpoons} \tag{R2a}$$

$$[(-\mathrm{OH})_\nu : \mathrm{Zn(C_2H_5)_2}]\langle \mathrm{s}\rangle \overset{i=2}{\rightleftharpoons} \tag{R2b}$$

$$[(-\mathrm{OH})_\nu : \mathrm{Zn(C_2H_5)_2}]^\ddagger\langle \mathrm{s}\rangle \overset{i=3}{\longrightarrow} \tag{R2c}$$

$$(-\mathrm{O}-)_\nu\mathrm{Zn(C_2H_5)_{2-\nu}}\langle \mathrm{s}\rangle + \nu\mathrm{C_2H_6}\langle \mathrm{g}\rangle$$

in which $\langle \mathrm{s}\rangle$ and $\langle \mathrm{g}\rangle$ denote the surface and gaseous species, respectively, and ν is the average number of hydroxyl groups that react with each $\mathrm{Zn(C_2H_5)_2}$ molecule (Elam and George, 2003; Yousfi et al., 2000). The adsorption and decomposition of $\mathrm{H_2O}$ at the $(-\mathrm{O}-)_\nu\mathrm{Zn(C_2H_5)_{2-\nu}}\langle \mathrm{s}\rangle$ surface site occur sequentially:

$$(-\mathrm{O}-)_\nu\mathrm{Zn(C_2H_5)_{2-\nu}}\langle \mathrm{s}\rangle + \mathrm{H_2O}\langle \mathrm{g}\rangle \overset{i=4}{\rightleftharpoons} \tag{R3a}$$

$$[(-\mathrm{O}-)_\nu\mathrm{Zn(C_2H_5)_{2-\nu}} : \mathrm{H_2O}]\langle \mathrm{s}\rangle \overset{i=5}{\rightleftharpoons} \tag{R3b}$$

$$[(-\mathrm{O}-)_\nu\mathrm{Zn(C_2H_5)_{2-\nu}} : \mathrm{H_2O}]^\ddagger\langle \mathrm{s}\rangle \overset{i=6}{\longrightarrow} \tag{R3c}$$

$$(-\mathrm{O}-)\mathrm{Zn}(-\mathrm{OH})_\nu\langle \mathrm{s}\rangle + (2-\nu)\mathrm{C_2H_6}\langle \mathrm{g}\rangle$$

It is assumed that the elimination reaction ($i = \{3, 6\}$) is irreversible in both half-reactions due to the removal of $\mathrm{C_2H_6}$, and that it is the rate-limiting step of the sequence of reactions. The intermediate complexes in Reactions (R2 and R3) have a significant adsorption energy, which becomes important at low temperatures ($T < 200$ (°C)), where the growth rate of the film can decrease significantly due to the stabilization of the adsorption complex (Ren, 2009). The apparent fall in MGPC at high temperatures is generally attributed to a gradual decrease in the density of the surface hydroxyl groups (Deminsky et al., 2004; Matero et al., 2000; Rahtu et al., 2001). This decrease results from an increase in the rate of the recombination reaction with increasing temperature. Reactions (R2 and R3), however, suppose that the entropy of the gas-phase precursor molecules increases significantly as the temperature increases, making desorption of the adsorbed precursor more favorable, and consequently lowering the equilibrium surface coverage. This causes the growth rate to fall (Travis and Adomaitis,

Table 2: Summary of gaseous and fractional surface coverage species in Reactions (R2 and R3), with their abbreviations.

Gaseous species ($\langle g \rangle$)	α	Surface species ($\langle s \rangle$)	κ
$Zn(C_2H_5)_2$	A	$(-OH)$	$A*$
H_2O	B	$[(-OH)_\nu : Zn(C_2H_5)_2]$	$B*$
C_2H_6	C	$[(-OH)_\nu : Zn(C_2H_5)_2]^\ddagger$	$C*$
N_2	P	$(-C_2H_5)_{2-\nu}$	$D*$
		$[(-O-)_\nu Zn(C_2H_5)_{2-\nu} : H_2O]$	$E*$
		$[(-O-)_\nu Zn(C_2H_5)_{2-\nu} : H_2O]^\ddagger$	$F*$

2013b; Widjaja and Musgrave, 2002a,b). Table 2 lists the abbreviations for the gaseous and fractional surface species in Reactions (R2 and R3).

4. Physical Modeling

The modeling of an ALD continuous flow reactor system can be performed at several levels of detail and with various assumptions (see e.g. (Aarik and Siimon, 1994; Yanguas-Gil and Elam, 2012; Ylilammi, 1995)). The level of detail chosen depends on the goal of the modeling, as defined by Hangos and Cameron (2001), and how the model is to be applied. Despite the diversity of published work in the field, the deposition process depends strongly on the characteristic time scales (Adomaitis, 2010; Granneman et al., 2007), on the underlying reactor-scale mass transport (Aarik et al., 2006; Jur and Parsons, 2011; Mousa et al., 2012), and on the reaction mechanism at the gas–surface interface (Ritala and Leskelä, 2002).

4.1. Formulation of Underlying Model Assumptions

The model described here was based on the two-dimensional model described in a recently published three-part article series (Holmqvist et al., 2012, 2013a,b). Several assumptions have been made in order to simplify the overall modeling framework and reduce the computational requirements, without sacrificing the accuracy and applicability of the model. Some of the assumptions arise from the

operation of the ALD reactor system (see Section 2.1), while others are based on theory (Holmqvist et al., 2012). The additional theory related assumptions made in the work presented here are:

i) That the one-dimensional representation of the spatial domain, $z \in [z_0, z_{\text{end}}]$, subject to fully developed channel flow with the z-axis coincident with the apex of the direction of the flow (Bird et al., 1960):

$$v_z(y) := v_{\text{z,max}}\Big(1 - \Big[\frac{y}{\delta y}\Big]^2\Big) \tag{4}$$

is sufficiently accurate. This assumption implies that the velocity of the flow in contact with the plates is zero, so that $v_z = 0$ at $y = \pm\delta y$, and $v_{z,\max} := (3/2)v_z$ (see Fig. 1b). Eq. (4) shows that the shear stress is:

$$\Phi_z = \frac{\partial}{\partial y}\Big(-\mu\frac{\partial v_z(y)}{\partial y}\Big) := \Big(\frac{3}{\delta y^2}\Big)\mu v_z \tag{5}$$

ii) That a steady-state representation of the reversible chemisorption of precursors ($i = \{1,\ 4\}$) in Reactions (R2 and R3) is sufficiently accurate, and that the reaction rates of the consecutive forward and reverse surface reactions ($i = \{2, 5\}$) establish a dynamic equilibrium.

4.2. Governing Equations of the ALD Reactor Sub-model

The mathematical model of the low-volume, continuous cross-flow ALD reactor with temporal precursor pulsing is based on fully coupled, compressible equations (Bird et al., 1960) for the conservation of mass, momentum, and individual gas-phase species defined in the one-dimensional spatial domain, $z \in [z_0, z_{\text{end}}]$. The model uses transient conditions for all governing equations in the temporal domain, $t \in [t_0, t_f]$, in order to capture details of the process dynamics at the level of a single ALD pulse sequence:

$$\frac{\partial \rho}{\partial t} = -\frac{\partial}{\partial z}\Big(\rho v_z\Big) + \sum_{\forall \alpha} S_\alpha \tag{6}$$

$$\rho\frac{\partial v_z}{\partial t} + v_z\frac{\partial \rho}{\partial t} = -\frac{\partial}{\partial z}\Big(\rho v_z v_z - \frac{4}{3}\mu\frac{\partial v_z}{\partial z} + p\Big) - \Phi_z \tag{7}$$

$$\rho\frac{\partial \omega_\alpha}{\partial t} + \omega_\alpha\frac{\partial \rho}{\partial t} = -\frac{\partial}{\partial z}\Big(\rho\omega_\alpha v_z - \rho\mathscr{D}_{\alpha\beta}\frac{\partial \omega_\alpha}{\partial z}\Big) + S_\alpha \tag{8}$$

in which ω_α denotes the mass fraction of the αth gas-phase species, and ρ is the density of the gas mixture. The pressure, p, is governed by the equation of state:

$$p = \frac{\rho}{\bar{M}} RT \tag{9}$$

$$\frac{1}{\bar{M}} = \sum_{\forall\alpha} \frac{\omega_\alpha}{M_\alpha} \tag{10}$$

The sum over all chemical reaction source terms, S_α, does not drop out in Eq. (6) because the total mass is not conserved in the ALD gas–surface reactions. The transport coefficients, $\mathscr{D}_{\alpha\beta}$ and μ_α, were determined from the Chapman–Enskog kinetic theory of dilute gases (Hirschfelder et al., 1964; Reid et al., 1988), while the viscosity for the multicomponent mixture of gases, μ, was determined using the semi-empirical mixing formula (Wilke, 1950).

4.2.1. Boundary Conditions

The inlet, $z = z_0$, boundary condition prescribes that the mass flow is a standard volumetric flow rate. Hence, the mass fluxes for each component and for the gas mixture, along with a Neumann condition on the velocity, are given by the equations:

$$(\rho v_z)\Big|_{z=z_0} = \frac{1}{A'} \sum_{\forall\alpha} \rho_{\mathrm{STP},\alpha} \dot{Q}_\alpha \Pi_\alpha(t, \Delta t_\alpha) \tag{11}$$

$$\frac{\partial v_z}{\partial z}\Big|_{z=z_0} = 0 \tag{12}$$

$$\left(\rho\omega_\alpha v_z - \rho\mathscr{D}_{\alpha\beta}\frac{\partial\omega_\alpha}{\partial z}\right)\Big|_{z=z_0} = \frac{1}{A'}\rho_{\mathrm{STP},\alpha}\dot{Q}_\alpha\Pi_\alpha(t, \Delta t_\alpha) \tag{13}$$

Moreover, the outlet, $z = z_{\mathrm{end}}$, boundary condition prescribes that the diffusive mass is zero, along with a Dirichlet condition on the velocity:

$$\frac{\partial\omega_\alpha}{\partial z}\Big|_{z=z_{\mathrm{end}}} = 0 \tag{14}$$

$$v_z\Big|_{z=z_{\mathrm{end}}} = \frac{\dot{V}_{\mathrm{VP}}}{A'} \tag{15}$$

where $\dot{V}_{\mathrm{VP}}$ denotes the constant flow rate for the vacuum pump (see Fig. 1a).

4.3. Governing Equations of the ALD Film Growth Sub-model

The general surface reaction model that describes the spatial and temporal fractional surface coverage is:

$$\frac{\partial \Lambda\theta_\kappa}{\partial t} = \sum_{i=1}^{N_i} \xi_{\kappa,i} r_i \tag{16a}$$

$$0 = \sum_{\forall\kappa} \frac{\partial \Lambda\theta_\kappa}{\partial t} \tag{16b}$$

where Λ denotes the maximum molar concentration of surface sites per unit substrate area that are available for deposition. The heterogeneous ALD gas–surface reactions mean that there will be a net mass consumption at the substrate surface, and thus the fractional surface coverage dynamics of Eq. (16) governs the source term, S_α, of the continuity equation for the precursor density (see also Eq. (8)):

$$S_\alpha = -\frac{A_{\text{sub}}}{V_{\text{RC}}} M_\alpha \Big[\sum_{\forall\kappa} \xi_{\alpha,\kappa} \frac{\partial \Lambda\theta_\kappa}{\partial t} - \sum_{i=1}^{N_i} \xi_{\kappa,i}^{\text{fwd}} r_i^{\text{fwd}} \Big] \tag{17}$$

where $\xi_{\alpha,\kappa}$ denotes the stoichiometric coefficient that corresponds to the αth species. Consequently, the mass accumulated from the adsorption/chemisorption of the precursor on the surface per unit QCM sensor area is given by:

$$\frac{d\langle m_q \rangle}{dt} = \frac{1}{(\zeta_{\text{end}} - \zeta_0)} \int_{\zeta_0}^{\zeta_{\text{end}}} \Big[\sum_{\forall\alpha} M_\alpha \sum_{\forall\kappa} \xi_{\alpha,\kappa} \frac{\partial \Lambda\theta_\kappa}{\partial t} + \sum_{i=1}^{N_i} \Delta M_i r_i^{\text{fwd}} \Big] d\zeta \tag{18}$$

in which $\zeta \in [\zeta_0, \zeta_{\text{end}}]$ is the spatial coordinate variable of the exposed quartz crystal surface. The mass gain in Eq. (18), for the integration limits $\zeta \in [z_0, z_{\text{end}}]$, equals the mass loss in Eq. (6): $V_{\text{RC}}(A_{\text{sub}})^{-1} \sum_{\forall\alpha} S_\alpha$.

Finally, the molar reaction rate of the ith elementary gas–surface and surface reaction in Eqs. (16–18) is given by the general formulation:

$$r_i^{\text{eq}} = k_i^{\text{ads}} p_\alpha \Big(\Lambda - \sum_{\forall\ell} \Lambda\theta_\ell \Big)^{n_i^{\text{ads}}} - k_i^{\text{des}} \Big(\Lambda\theta_\kappa \Big)^{n_i^{\text{des}}} \tag{19a}$$

$$r_i^{\text{fwd}} = k_i^{\text{fwd}} \Big(\Lambda\theta_\kappa \Big)^{n_i^{\text{fwd}}} \tag{19b}$$

in which the subscript ℓ represents all κth surface species with which the αth gaseous species cannot undergo a reaction, n_i^{ads} is the adsorption order related to the interaction between adsorbents, and n_i^{des} is the corresponding desorption order. Hence, imposing the equilibrium relationship, $r_i^{\text{eq}} := 0$, allows to rewrite Eq. (19a) as (introducing $K_i^{\text{eq}} = k_i^{\text{ads}}(k_i^{\text{des}})^{-1}$):

$$0 = K_i^{\text{eq}} p_\alpha \Big(\Lambda - \sum_{\forall \ell} \Lambda\theta_\ell\Big)^{n_i^{\text{ads}}} - \Big(\Lambda\theta_\kappa\Big)^{n_i^{\text{des}}} \tag{19c}$$

The temperature dependency of the forward, k_i^{fwd}, adsorption, k_i^{ads}, and desorption, k_i^{des}, rate constants is governed by reparameterization of the Arrhenius equation by introducing a reference temperature, $T_{\text{ref},i}$, in the form (Schwaab et al., 2008; Schwaab and Pinto, 2007, 2008):

$$k_i = k_{T_{\text{ref}},i} \exp\Big(-\frac{E_i}{R}\Big[\frac{1}{T} - \frac{1}{T_{\text{ref},i}}\Big]\Big) \tag{20a}$$

$$k_{T_{\text{ref}},i} = A_i \exp\Big(-\frac{E_i}{R}\frac{1}{T_{\text{ref},i}}\Big) \tag{20b}$$

where $k_{T_{\text{ref}},i}$ is the specific reaction rate coefficient at $T_{\text{ref},i}$, A_i is the frequency factor, and E_i is the activation energy of the ith elementary reaction. The expression for chemical reactions in equilibrium is thus:

$$K_i^{\text{eq}} = \frac{k_i^{\text{ads}}}{k_i^{\text{des}}} = K_{T_{\text{ref}},i}^{\text{eq}} \exp\Big(-\frac{\Delta E_i^{\text{eq}}}{R}\Big[\frac{1}{T} - \frac{1}{T_{\text{ref},i}^{\text{eq}}}\Big]\Big) \tag{20c}$$

in which $K_{T_{\text{ref}},i}^{\text{eq}} := k_{T_{\text{ref}},i}^{\text{ads}}(k_{T_{\text{ref}},i}^{\text{des}})^{-1}$, $\Delta E_i^{\text{eq}} := E_i^{\text{ads}} - E_i^{\text{des}}$, and $T_{\text{ref},i}^{\text{eq}} := T_{\text{ref},i}^{\text{ads}} = T_{\text{ref},i}^{\text{des}}$.

4.3.1. Surface State Limit-cycle Dynamics

The differential-algebraic equation (DAE) system that governs the fractional surface-coverage species, θ_κ, and that gives the dynamics for both ALD half-

reactions (Reactions (R2 and R3)) is:

$$\xi^{\mathrm{eq}}_{B*,1}\frac{\partial \Lambda\theta_{A*}}{\partial t}+\xi^{\mathrm{eq}}_{A*,1}\frac{\partial \Lambda\theta_{B*}}{\partial t}=-\xi^{\mathrm{eq}}_{A*,1}\xi^{\mathrm{eq}}_{B*,2}r^{\mathrm{eq}}_{2}+\xi^{\mathrm{eq}}_{B*,1}\xi^{\mathrm{fwd}}_{A*,6}r^{\mathrm{fwd}}_{6} \tag{21a}$$

$$\frac{\partial \Lambda\theta_{C*}}{\partial t}=\ \xi^{\mathrm{eq}}_{C*,2}r^{\mathrm{eq}}_{2}-\xi^{\mathrm{fwd}}_{C*,3}r^{\mathrm{fwd}}_{3} \tag{21b}$$

$$\xi^{\mathrm{eq}}_{E*,4}\frac{\partial \Lambda\theta_{D*}}{\partial t}+\xi^{\mathrm{eq}}_{D*,4}\frac{\partial \Lambda\theta_{E*}}{\partial t}=-\xi^{\mathrm{eq}}_{D*,4}\xi^{\mathrm{eq}}_{E*,5}r^{\mathrm{eq}}_{5}+\xi^{\mathrm{eq}}_{E*,4}\xi^{\mathrm{fwd}}_{D*,3}r^{\mathrm{fwd}}_{3} \tag{21c}$$

$$\frac{\partial \Lambda\theta_{F*}}{\partial t}=\ \xi^{\mathrm{eq}}_{F*,5}r^{\mathrm{eq}}_{5}-\xi^{\mathrm{fwd}}_{F*,6}r^{\mathrm{fwd}}_{6} \tag{21d}$$

$$0=K^{\mathrm{eq}}_{1}p_{A}\big(\Lambda\theta_{A*}\big)^{n^{\mathrm{ads}}_{1}}-\big(\Lambda\theta_{B*}\big)^{n^{\mathrm{des}}_{1}} \tag{21e}$$

$$0=K^{\mathrm{eq}}_{4}p_{B}\big(\Lambda\theta_{D*}\big)^{n^{\mathrm{ads}}_{4}}-\big(\Lambda\theta_{E*}\big)^{n^{\mathrm{des}}_{4}} \tag{21f}$$

The sum of Eqs. (21a–21d) is zero, and Eq. (16b) is thus fulfilled. Furthermore, the mathematical formulation of the ith equilibrium, r^{eq}_{i}, and forward reactions rates, r^{fwd}_{i}, (see Eq. (19)) in Eq. (21) are:

$$r^{\mathrm{eq}}_{2}=k^{\mathrm{fwd}}_{2}\big(\Lambda\theta_{B*}\big)^{n^{\mathrm{fwd}}_{2}}-k^{\mathrm{rev}}_{2}\big(\Lambda\theta_{C*}\big)^{n^{\mathrm{rev}}_{2}} \tag{22a}$$

$$r^{\mathrm{eq}}_{5}=k^{\mathrm{fwd}}_{5}\big(\Lambda\theta_{E*}\big)^{n^{\mathrm{fwd}}_{5}}-k^{\mathrm{rev}}_{5}\big(\Lambda\theta_{F*}\big)^{n^{\mathrm{rev}}_{5}} \tag{22b}$$

$$r^{\mathrm{fwd}}_{3}=k^{\mathrm{fwd}}_{3}\big(\Lambda\theta_{C*}\big)^{n^{\mathrm{fwd}}_{3}} \tag{22c}$$

$$r^{\mathrm{fwd}}_{6}=k^{\mathrm{fwd}}_{6}\big(\Lambda\theta_{F*}\big)^{n^{\mathrm{fwd}}_{6}} \tag{22d}$$

It is, however, worth noting that Eq. (21) must be reformulated before the dynamic optimization problem is considered. The remaining kinetic parameters, including the specific reaction rate at $T_{\mathrm{ref},i}$, $k_{T_{\mathrm{ref}},i}$, and the associated activation energy, E_i, for the ith elementary surface reaction (Reactions (R2 and R3)) can be gathered into a calibration parameter vector $\boldsymbol{\beta}\in\mathbb{R}^{N_\beta}$:

$$\boldsymbol{\beta}=[K^{\mathrm{eq}}_{T_{\mathrm{ref}},\imath},\Delta E^{\mathrm{eq}}_{\imath},k^{\mathrm{fwd}}_{T_{\mathrm{ref}},\jmath},E^{\mathrm{fwd}}_{\jmath},k^{\mathrm{rev}}_{T_{\mathrm{ref}},\ell},E^{\mathrm{rev}}_{\ell}]^{T} \tag{23}$$

where $\imath\in\{1,4\}$, $\jmath\in\{2,3,5,6\}$, $\ell\in\{2,5\}$, and where $\mathbf{T}_{\mathrm{ref}}=[T^{\mathrm{eq}}_{\mathrm{ref},\imath},T^{\mathrm{fwd}}_{\mathrm{ref},\jmath},T^{\mathrm{rev}}_{\mathrm{ref},\ell}]^{T}$ is a vector that collects all reference temperatures. Finally, all exponential factors, n_i, are set to unity and the stoichiometric coefficients $\xi_{\kappa,i}$ and $\forall i$ associated with the ith elementary gas–surface and surface reaction are defined according to Reactions (R2 and R3).

4.4. Limit-cycle Solutions

The ALD reactor sub-model and film growth sub-model described above can be used to study the dynamic nature of precursor pulsation and the resulting film growth process as a function of surface state initial conditions and process operating parameters. However, computing the limit-cycle solution over the time horizon $[t_0, t_f]$ requires one additional important criterion; that the state of the surface returns to its initial condition at the end of the cycle, $t = t_f$ (Travis and Adomaitis, 2013a,b):

$$\theta_\kappa(t_0) := \theta_\kappa(t_f), \qquad \forall \kappa \in \{A*, \cdots, F*\} \tag{24a}$$

In addition, the non-differentiated form of Eq. (16b) must be satisfied at $t \in \{t_0, t_f\}$:

$$1 = \sum_{\forall \kappa} \theta_\kappa(t) \tag{24b}$$

Eq. (24b) reduces the number of free variables of the initial equations to $N_\kappa - 1$. Section 6 presents numerical aspects of computing limit-cycle solutions.

4.5. Model Form and Size

The non-linear partial differential algebraic equations (PDAEs) of the ALD reactor sub-model (see Section 4.2) and the film growth sub-model (see Section 4.3) were approximated using the method-of-lines (Davis, 1984; Schiesser, 1991) and the finite volume method (FVM). In this study, FVM was used mainly due to its mass conservation property (Fornberg, 1988) and because it is easy to implement, in particular at the system boundaries. The first-order spatial derivative of the density, ρ, in Eq. (6) and of the gas-phase mass fractions, ω_α, in Eq. (8) have been approximated using a first-order downwind discretization scheme, while a first-order upwind discretization scheme was utilized to approximate the bulk velocity, v_z, in Eq. (7), yielding a large system of non-linear differential algebraic equations. Thus, the process model may be written

collectively as a general non-linear index-1 DAE system as:

$$\mathbf{0} = \mathbf{F}(\dot{\mathbf{x}}(t), \mathbf{x}(t), \mathbf{u}(t), \mathbf{w}(t), \boldsymbol{\beta}) \tag{25a}$$

$$\mathbf{0} = \mathbf{F}_0(\dot{\mathbf{x}}(t_0), \mathbf{x}(t_0), \mathbf{u}(t_0), \mathbf{w}(t_0), \boldsymbol{\beta}) \tag{25b}$$

$$\mathbf{0} = \mathbf{C_e}(t_0, t_f, \mathbf{x_e}, \mathbf{u_e}, \mathbf{w_e}, \boldsymbol{\beta}) \tag{25c}$$

$$\mathbf{x}(t_0) = \mathbf{x}_0 \tag{25d}$$

in which $\mathbf{F}$ is the DAE that represents the dynamics of the system, $\mathbf{F}_0$ represent the DAE augmented with initial conditions, and $\mathbf{C_e}$ is a point equality-constraint function that assures that the limit-cycle criterion (see Eq. (24a)) is fulfilled. Finally, $\mathbf{x}$, $\mathbf{u}$ and $\mathbf{w}$ represent dependent states, free design variables (see Section 2.1), and algebraic variables:

$$\mathbf{x} = [\rho, v_z, \omega_\alpha, \theta_\kappa, m_q]^T, \qquad \alpha \in \{A, B, C\}, \kappa \notin \{B*, E*\}$$

$$\mathbf{w} = [p, \bar{M}, \theta_\kappa]^T, \qquad \kappa \in \{B*, E*\}$$

$$\mathbf{y} = \langle m_q \rangle$$

$$\mathbf{u} = [\Delta t_\alpha, \dot{Q}_\alpha, T, \dot{V}_{\mathrm{VP}}]^T, \qquad \alpha \in \{A, B, P\}$$

Consequently, when the number of FVM elements, N_{FVM}, is 20, the number of states, N_x, is $10N_{\mathrm{FVM}}$ and the number of algebraic variables, N_w, is $4N_{\mathrm{FVM}}$. The number of FVM elements is a compromise between accuracy and computational complexity, and gives adequate representation of the dispersion.

5. Dynamic Parameter Estimation

5.1. Non-convex Dynamic Optimization Problem Formulation

The dynamic parameter estimation problem aims to solve for the calibration parameter vector, $\boldsymbol{\beta} \in \mathbb{R}^{N_\beta}$, of the dynamic model outlined in Section 4, supplied as a fully implicit DAE system (see Eq. (25)). Thus, this problem can be formulated as a general dynamic optimization problem (DOP) over the time interval $[t_0, t_f]$, with differential algebraic constraints (Biegler, 2010; Biegler

et al., 2002) of the form:

$$\min_{\boldsymbol{\beta}\in\mathbb{R}^{N_\beta}} \; \Phi(\boldsymbol{\beta}) \tag{26}$$

$$\begin{aligned} \text{subj. to} \quad & \text{Eq. (25)} \\ & \mathbf{y} = \mathbf{g}_{\mathbf{y}}(\mathbf{x}(t), \mathbf{u}(t), \mathbf{w}(t), \boldsymbol{\beta}) \\ & \mathbf{x}_{\min} \leq \mathbf{x} \leq \mathbf{x}_{\max}, \qquad \mathbf{w}_{\min} \leq \mathbf{w} \leq \mathbf{w}_{\max} \\ & \mathbf{u}_{\min} \leq \mathbf{u} \leq \mathbf{u}_{\max}, \qquad \boldsymbol{\beta}_{\min} \leq \boldsymbol{\beta} \leq \boldsymbol{\beta}_{\max} \end{aligned}$$

in which the response function, $\mathbf{g}_{\mathbf{y}}$, transforms and selects those state variables that are experimentally measured, and where $\boldsymbol{\beta}$ is subject to lower and upper bounds acting as inequality constraints, and estimated by minimizing an objective function $\Phi\big(\boldsymbol{\beta}\big)$, penalizing deviations between the observed, $\hat{\mathbf{y}}$, and the predicted system response, $\mathbf{y}$. The weighted sum of squared residuals is used to quantify the estimation, and is defined as:

$$\Phi(\boldsymbol{\beta}) = \int_{t_0}^{t_f} \big[\hat{\mathbf{y}}(t) - \mathbf{y}(t, \mathbf{x}, \mathbf{u}, \boldsymbol{\beta}, \mathbf{w})\big]^T \mathbf{W} \big[\hat{\mathbf{y}}(t) - \mathbf{y}(t, \mathbf{x}, \mathbf{u}, \boldsymbol{\beta}, \mathbf{w})\big] dt \tag{27}$$

where the diagonal weight matrix, $\mathbf{W}$, is introduced to normalize the experimental response, $\hat{\mathbf{y}}(t)$, and penalize a deviation with its associated variance, $\sigma^2_{\hat{\mathbf{y}}}(t)$.

5.2. Optimal Reparameterization of the Arrhenius Equation

The mathematical structure of the non-linear Arrhenius equation (see Eq. (20)) introduces a high correlation between the frequency factor, A_i, and the activation energy, E_i (Schwaab and Pinto, 2007). This may cause significant numerical problems when estimating the model parameters and may lead to the statistical significance of the final parameter estimates being misinterpreted (Watts, 1994). Schwaab et al. (2008) showed that the explicit introduction of a reference temperature into the standard Arrhenius equation and proper selection of the set of reference temperatures, $\mathbf{T}_{\text{ref}} \in \mathbb{R}^{N_i}$, in problems involving multiple Arrhenius equations can minimize the correlations between parameter

estimates, and minimize at the same time the relative standard errors of the parameter estimates. The two-step parameter estimation procedure proposed by Schwaab et al. (2008) was for this reason used in this study. This procedure comprises:

i) Solution of the DOP (see Eq. (27)) using the initial guesses for $\mathbf{T}_{\text{ref}}$ as the average temperature values in the analyzed experimental range (Vegliò et al., 2001).

ii) Minimization of the L_2-norm of the correlation matrix, $\mathbf{C}(\hat{\boldsymbol{\beta}}, \mathbf{T}_{\text{ref}})$, of parameter estimates, $\hat{\boldsymbol{\beta}}$:

$$\min_{\mathbf{T}_{\text{ref}} \in \mathbb{R}^{N_i}} \|\mathbf{C}(\hat{\boldsymbol{\beta}}, \mathbf{T}_{\text{ref}})\|_2 \tag{28}$$
$$\text{subj. to} \quad \mathbf{T}_{\text{ref,min}} \leq \mathbf{T}_{\text{ref}} \leq \mathbf{T}_{\text{ref,max}}$$

iii) Re-optimization of the DOP with the optimized set of reference temperatures from Eq. (28).

The correlation matrix in Eq. (28) is determined from the covariance matrix of the parameter estimates, $\boldsymbol{\Sigma}(\hat{\boldsymbol{\beta}}, \mathbf{T}_{\text{ref}}) = s^2\left[\mathbf{J}(\hat{\boldsymbol{\beta}}, \mathbf{T}_{\text{ref}})^T \mathbf{W} \mathbf{J}(\hat{\boldsymbol{\beta}}, \mathbf{T}_{\text{ref}})\right]^{-1}$ (Bates and Watts, 1988; Draper and Smith, 1998):

$$\mathbf{C}_{\imath\ell}(\hat{\boldsymbol{\beta}}, \mathbf{T}_{\text{ref}}) = \frac{\boldsymbol{\Sigma}_{\imath\ell}(\hat{\boldsymbol{\beta}}, \mathbf{T}_{\text{ref}})}{\left[\boldsymbol{\Sigma}_{\imath\imath}(\hat{\boldsymbol{\beta}}, \mathbf{T}_{\text{ref}}) \boldsymbol{\Sigma}_{\ell\ell}(\hat{\boldsymbol{\beta}}, \mathbf{T}_{\text{ref}})\right]^{1/2}}, \qquad \forall \imath, \ell \in \{1, 2, \cdots, N_\beta\} \tag{29}$$

Additionally, it is convenient to update the covariance matrix, $\boldsymbol{\Sigma}(\hat{\boldsymbol{\beta}}, \mathbf{T}_{\text{ref}})$, at each set $\mathbf{T}_{\text{ref}}$ using the explicit method presented by Rimensberger and Rippin (1986).

6. Modeling and Optimization Environment

6.1. Discretization Procedure for Limit-cycle System Dynamics

The collocation algorithm in the open-source platform JModelica.org (Åkesson et al., 2010) was used to compute the stable limit-cycle dynamic solution to the process model (see Eq. (25)). The system dynamics (see Eq. (25a)) were described using the Modelica language (The Modelica Association, 2012), which

is a high-level language for complex physical models, while the limit-cycle criterion (see Eq. (25c)) was implemented in the Modelica extension Optimica (Åkesson, 2008). The user interacts with the various components of JModelica.org through the Python scripting language. JModelica.org contains implementations of Legendre–Gauss and Legendre–Gauss–Radau collocation schemes on finite elements. In this study, state and algebraic variables were parameterized by Lagrange polynomials of order three and two, respectively, based on Radau collocation points. This gave a non-linear program (NLP) with structure, which was exploited by the solver IPOPT (Wächter and Biegler, 2006). IPOPT uses a sparse primal-dual interior point method to find local optima of large-scale NLPs.

The first and second-order derivatives of the constraints functions with respect to the NLP variables were computed using the computer algebra system with automatic differentiation (CasADi) (Andersson et al., 2012a) in order to enhance the performance of IPOPT, especially the speed at which the algorithm converged (see e.g. Magnusson and Åkesson (2012)). CasADi is a minimalistic computer algebra system that implements automatic differentiation (AD) in the forward and adjoint modes using a hybrid symbolic/numeric approach. Once a symbolic representation has been created using CasADi, the derivatives that are required are efficiently and conveniently obtained, and sparsity patterns are preserved.

6.2. Sequential Parameter Estimation Methodology

Parameter estimation methods can be classified into two classes: direct search methods and gradient methods (Edgar and Himmelblau, 1988). The model-based methodology described here solved the DOP (see Eq. 26) as follows: First, the parameter space, $\mathbb{R}^{N_\beta}$, was sampled by Latin hypercube sampling (LHS) (McKay et al., 1979) to obtain suitable input for the heuristic optimization method. Subsequently, the evolution strategy Differential Evolution (DE) *DE/rand-to-best/2/bin* (Price, 1999; Storn and Price, 1997) was used to find the optimal least-squares estimates. Gradient methods generally outper-

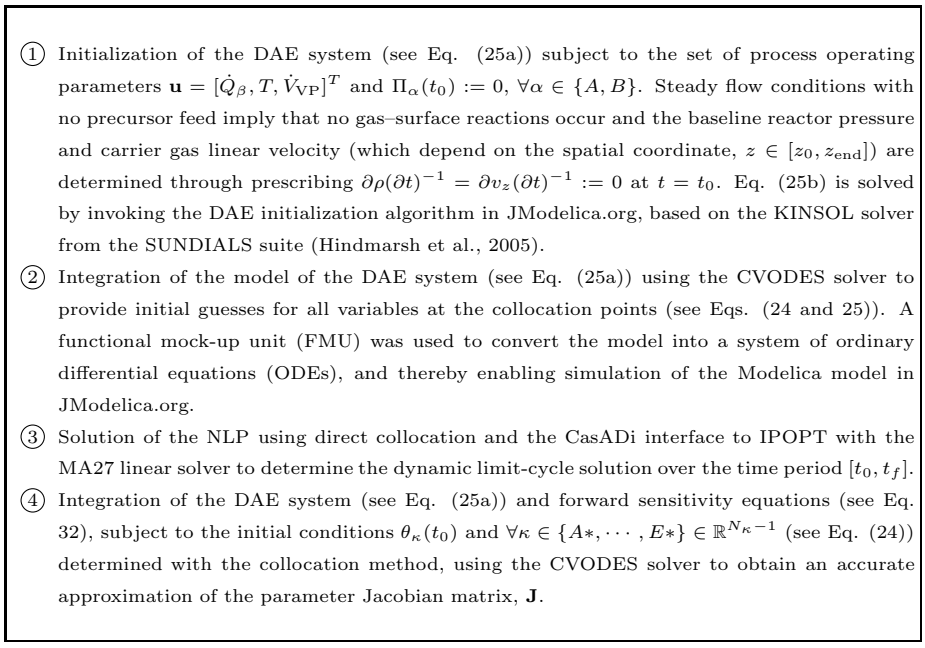

Figure 3: The discretization procedure for limit-cycle system dynamics and the sequential parameter estimation method. The final step is invoked only when verifying the solution from the collocation method that precedes it, and when executing the Levenberg–Marquardt algorithm (see Eq. (31)).

form direct search methods both in terms of reliability and speed of convergence (Bard, 1974). Therefore, in order to ensure reliability and to promote convergence of the optimal calibration parameter vector, $\boldsymbol{\beta}^*$, from DE with respect to the feasible region (the region in which the parameters are linearly independent):

$$\left\{\boldsymbol{\beta}^* \in \mathbb{R}^{N_\beta} \;:\; \mathrm{rank}(\mathbf{J}(\boldsymbol{\beta}^*)) = N_\beta \;\wedge\; \neg\exists \boldsymbol{\beta} \in \mathbb{R}^{N_\beta},\; \Phi(\boldsymbol{\beta}) \leq \Phi(\boldsymbol{\beta}^*)\right\} \tag{30}$$

the Levenberg–Marquardt algorithm (LMA) was used to give the final least-squares estimates, $\hat{\boldsymbol{\beta}}$. The LMA developed for this modeling framework (Andersson et al., 2012b) uses a search direction that is the solution of the set of linear equations:

$$\left[\mathbf{J}^T\mathbf{W}\mathbf{J} + \lambda \mathrm{diag}(\mathbf{J}^T\mathbf{W}\mathbf{J})\right]\boldsymbol{\delta}_\beta = \mathbf{J}^T\mathbf{W}[\hat{\mathbf{y}} - \mathbf{y}] \tag{31}$$

in which $\mathbf{J} = \partial\mathbf{y}(\partial\boldsymbol{\beta})^{-1}$ is the parameter Jacobian matrix, $\boldsymbol{\delta}_\beta$ denotes an increment to the parameter vector, $\boldsymbol{\beta}$, and the damping factor, λ, controls both

the magnitude and direction of $\boldsymbol{\beta}$. The solution sensitivity with respect to the model parameters was used to obtain an accurate approximation of the parameter Jacobian matrix by means of the following forward sensitivity equations:

$$\frac{d}{dt}\left(\frac{\partial \mathbf{x}}{\partial \boldsymbol{\beta}}\right) = \frac{\partial \mathbf{F}}{\partial \mathbf{x}}\left(\frac{\partial \mathbf{x}}{\partial \boldsymbol{\beta}}\right) + \frac{\partial \mathbf{F}}{\partial \boldsymbol{\beta}}, \quad \frac{\partial \mathbf{x}(t_0)}{\partial \boldsymbol{\beta}} = \frac{\partial \mathbf{x}_0}{\partial \boldsymbol{\beta}} \tag{32}$$

obtained by applying the chain rule of differentiation to the original DAEs (see Eq. (25)). Eq. (32) introduces $(N_x \times N_\beta)$ new differential equations. Fig. 3 describes the collocation procedure used to solve forced periodic systems and the sequential parameter estimation method.

7. Results and Discussion

7.1. Accuracy and Reliability of the Parameter Estimates

The kinetic parameters (see Eq. (23)) involved in the ALD gas–surface reactions were estimated using the hybrid numerical procedure described in Section 6.2. The associated set of reference temperatures was subsequently optimized by means of the procedure described in Section 5.2, in order to minimize the parameter correlations. Table 3 lists the optimal set of parameter estimates, $\hat{\boldsymbol{\beta}}$, and reference temperatures, $\hat{\mathbf{T}}_{\mathrm{ref}}$, along with corresponding approximate margin of error, $\varepsilon_{\hat{\boldsymbol{\beta}}_\imath} = \boldsymbol{\Sigma}_{\imath\imath}(\hat{\boldsymbol{\beta}}, \hat{\mathbf{T}}_{\mathrm{ref}})^{1/2} t_{(\varphi;1-\alpha/2)}$, with a significance level of $\alpha = 5.0{\cdot}10^{-2}$ and $\forall \imath \in \{1, 2, \cdots, N_\beta\}$.

Fig. 4 shows representative results for these quantities for the kinetic parameters $\boldsymbol{\beta}_\imath$ and $\imath \in \{1, 2, 7, 8\}$ associated with Reactions (R2a and R2c) as functions of the reference temperatures $T^{\mathrm{eq}}_{\mathrm{ref},1}$ and $T^{\mathrm{fwd}}_{\mathrm{ref},3}$. These results show the behavior of the relative errors and the correlations between the parameter estimates. Figs. 4a and 4b show that the correlation between the parameters ΔE^{eq}_1 and E^{fwd}_3, and the relative errors of these, were independent of the reference temperature, as Schwaab and Pinto (2007) have shown previously. Further, the relative error of parameter $K^{\mathrm{eq}}_{T_{\mathrm{ref}},1}$ depended only on $T^{\mathrm{eq}}_{\mathrm{ref},1}$, while the relative error of parameter $k^{\mathrm{fwd}}_{T_{\mathrm{ref}},3}$ depended only on $T^{\mathrm{fwd}}_{\mathrm{ref},3}$. This is evident from Fig. 4b, from which it is also clear that the relative errors attained minimum values

Table 3: Regression analysis of the least-squares estimates, $\hat{\boldsymbol{\beta}}$, of the parameters of Reactions (R2 and R3). The normalized margin of error, $\bar{\varepsilon}_{\hat{\boldsymbol{\beta}}}$, was determined at a significance level of $\alpha = 5.0 \cdot 10^{-2}$. The specific reaction rate coefficients $K^{\mathrm{eq}}_{T_{\mathrm{ref}},\imath}, k^{\mathrm{fwd}}_{T_{\mathrm{ref}},\imath}$, and $k^{\mathrm{rev}}_{T_{\mathrm{ref}},\imath}$ are defined at the associated optimal reference temperature $T^{\mathrm{eq}}_{\mathrm{ref},\imath}$, $T^{\mathrm{fwd}}_{\mathrm{ref},\imath}$ and $T^{\mathrm{rev}}_{\mathrm{ref},\imath}$, respectively.

Elementary surface reaction, i	$\imath$	Parameter, $\boldsymbol{\beta}$	Parameter units	Parameter estimates, $\hat{\boldsymbol{\beta}}$	Margin of error, $\bar{\varepsilon}_{\hat{\boldsymbol{\beta}}}$ (%)
Reaction (R2a)	1	$K^{\mathrm{eq}}_{T_{\mathrm{ref}},1}$	Pa^{-1}	$4.97 \cdot 10^{-2}$	6.96
$A* + A \overset{K^{\mathrm{eq}}_1}{\rightleftharpoons} B*$	2	ΔE^{eq}_1	$\mathrm{J\,mol}^{-1}$	$4.48 \cdot 10^{4}$	5.98
		$T^{\mathrm{eq}}_{\mathrm{ref},1}$	K	$4.23 \cdot 10^{2}$	
Reaction (R2b)	3	$k^{\mathrm{fwd}}_{T_{\mathrm{ref}},2}$	s^{-1}	$1.61 \cdot 10^{2}$	1.82
$B* \underset{k^{\mathrm{rev}}_2}{\overset{k^{\mathrm{fwd}}_2}{\rightleftharpoons}} C*$	4	E^{fwd}_2	$\mathrm{J\,mol}^{-1}$	$4.22 \cdot 10^{4}$	1.75
		$T^{\mathrm{fwd}}_{\mathrm{ref},2}$	K	$4.10 \cdot 10^{2}$	
	5	$k^{\mathrm{rev}}_{T_{\mathrm{ref}},2}$	s^{-1}	$5.14 \cdot 10^{2}$	2.12
	6	E^{rev}_2	$\mathrm{J\,mol}^{-1}$	$9.51 \cdot 10^{4}$	6.01
		$T^{\mathrm{rev}}_{\mathrm{ref},2}$	K	$4.35 \cdot 10^{2}$	
Reaction (R2c)	7	$k^{\mathrm{fwd}}_{T_{\mathrm{ref}},3}$	s^{-1}	$3.72 \cdot 10^{1}$	5.34
$C* \xrightarrow{k^{\mathrm{fwd}}_3} D* + C$	8	E^{fwd}_3	$\mathrm{J\,mol}^{-1}$	$1.53 \cdot 10^{4}$	9.55
		$T^{\mathrm{fwd}}_{\mathrm{ref},3}$	K	$4.43 \cdot 10^{2}$	
Reaction (R3a)	9	$K^{\mathrm{eq}}_{T_{\mathrm{ref}},4}$	Pa^{-1}	$7.45 \cdot 10^{-2}$	1.60
$D* + B \overset{K^{\mathrm{eq}}_4}{\rightleftharpoons} E*$	10	ΔE^{eq}_4	$\mathrm{J\,mol}^{-1}$	$4.11 \cdot 10^{4}$	9.26
		$T^{\mathrm{eq}}_{\mathrm{ref},4}$	K	$4.24 \cdot 10^{2}$	
Reaction (R3b)	11	$k^{\mathrm{fwd}}_{T_{\mathrm{ref}},5}$	s^{-1}	$1.42 \cdot 10^{2}$	2.29
$E* \underset{k^{\mathrm{rev}}_5}{\overset{k^{\mathrm{fwd}}_5}{\rightleftharpoons}} F*$	12	E^{fwd}_5	$\mathrm{J\,mol}^{-1}$	$4.13 \cdot 10^{4}$	8.77
		$T^{\mathrm{fwd}}_{\mathrm{ref},5}$	K	$4.04 \cdot 10^{2}$	
	13	$k^{\mathrm{rev}}_{T_{\mathrm{ref}},5}$	s^{-1}	$3.76 \cdot 10^{2}$	1.79
	14	E^{rev}_5	$\mathrm{J\,mol}^{-1}$	$9.74 \cdot 10^{4}$	1.65
		$T^{\mathrm{rev}}_{\mathrm{ref},5}$	K	$4.39 \cdot 10^{2}$	
Reaction (R3c)	15	$k^{\mathrm{fwd}}_{T_{\mathrm{ref}},6}$	s^{-1}	$4.53 \cdot 10^{1}$	1.56
$F* \xrightarrow{k^{\mathrm{fwd}}_6} A* + C$	16	E^{fwd}_6	$\mathrm{J\,mol}^{-1}$	$2.97 \cdot 10^{4}$	4.28
		$T^{\mathrm{fwd}}_{\mathrm{ref},6}$	K	$4.40 \cdot 10^{2}$	

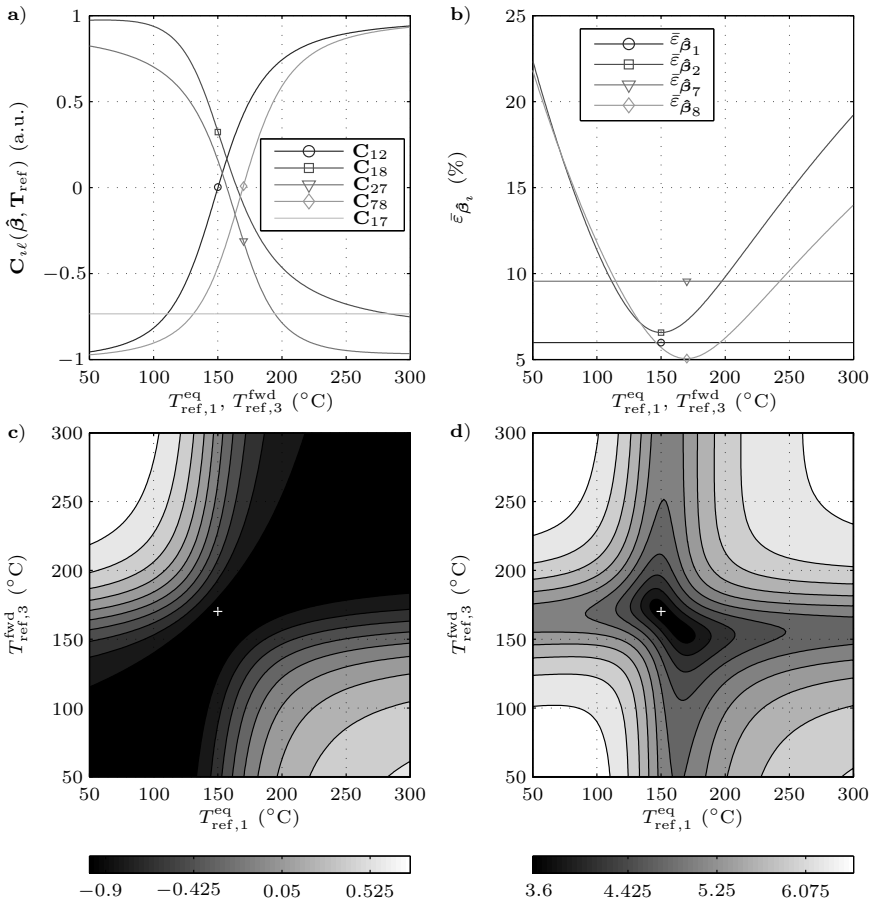

Figure 4: Representative results of the two-step procedure by which parameters were estimated, to be used for optimal reparameterization of the Arrhenius equation (Schwaab et al., 2008). a) $\mathbf{C}_{\iota\ell}(\hat{\boldsymbol{\beta}}, \mathbf{T}_{\mathrm{ref}})$ and $\iota \neq \ell$ as functions of $\mathbf{T}_{\mathrm{ref},i}$ and $i \in \{1, 3\}$. b) Relative errors, $\bar{\varepsilon}_{\hat{\boldsymbol{\beta}}_\iota}$, as functions of $\mathbf{T}_{\mathrm{ref},i}$. c) Correlation between $K^{\mathrm{eq}}_{T_{\mathrm{ref}},1}$ and $k^{\mathrm{fwd}}_{T_{\mathrm{ref}},3}$, $\mathbf{C}_{17}$, as a function of $\mathbf{T}_{\mathrm{ref},i}$. d) $\|\mathbf{C}(\hat{\boldsymbol{\beta}}, \mathbf{T}_{\mathrm{ref}})\|_2$ as a function of $\mathbf{T}_{\mathrm{ref},i}$. (+) Optimal set of reference temperatures $\hat{\mathbf{T}}_{\mathrm{ref},i}$ and $i \in \{1, 3\}$.

around certain values of $\mathbf{T}_{\mathrm{ref},i}$ and $i \in \{1, 3\}$. Fig. 4a shows also that the correlation coefficients associated with $K^{\mathrm{eq}}_{T_{\mathrm{ref}},1}$, i.e. $\mathbf{C}_{12}$ and $\mathbf{C}_{18}$, depended only on $T^{\mathrm{eq}}_{\mathrm{ref},1}$, whereas the correlation coefficients associated with $k^{\mathrm{fwd}}_{T_{\mathrm{ref}},3}$, i.e. $\mathbf{C}_{27}$ and $\mathbf{C}_{78}$, depend only on $T^{\mathrm{fwd}}_{\mathrm{ref},3}$. It is evident that these correlations can be made

equal to zero: $\mathbf{C}_{12}$ and $\mathbf{C}_{27}$, in particular, are approximately zero for the optimal values of $\mathbf{T}_{\mathrm{ref},i}$ and $i \in \{1,3\}$. Unfortunately, the optimal reference values do not lead to zero values of the correlations for the remaining coefficients $\mathbf{C}_{18}$ and $\mathbf{C}_{27}$ in Fig. 4a. Finally, the correlation between $K^{\mathrm{eq}}_{T_{\mathrm{ref}},1}$ and $k^{\mathrm{fwd}}_{T_{\mathrm{ref}},3}$, $\mathbf{C}_{17}$ depended in a complex manner on both $T^{\mathrm{eq}}_{\mathrm{ref},1}$ and $T^{\mathrm{fwd}}_{\mathrm{ref},3}$ (Fig. 4c). In addition $\mathbf{C}_{17}$ became very high at the optimal reference temperatures that minimize the L_2-norm of $\mathbf{C}(\hat{\boldsymbol{\beta}}, \mathbf{T}_{\mathrm{ref}})$ (see Eq. (28)) as depicted in Fig. 4d, and this allows other parameter correlations to be eliminated. Thus, it is clear that it is not possible to eliminate all correlations simultaneously.

Analysis of the confidence intervals and regions provides a more rigorous statistical evaluation of the parameter estimates. A statement with a high confidence suggests either that a parameter estimate cannot be discriminated from another using the experimental design being considered, or that there is a high uncertainty in the precision associated with this parameter (in other words: the model cannot distinguish between phenomenon in the system (Bard, 1974; Bates and Watts, 1988)). For this purpose, the likelihood $100(1-\alpha)\%$ joint confidence region is defined for all values of $\boldsymbol{\beta}$ such that:

$$\left\{\boldsymbol{\beta}:\ \Phi(\boldsymbol{\beta}) - \Phi(\hat{\boldsymbol{\beta}}) \leq s^2 N_\beta F_{(N_\beta,\varphi;\alpha)}\right\} \tag{33}$$

in which $F_{(N_\beta,\varphi;\alpha)}$ is the upper α quantile of Fisher's F-distribution. Fig. 5 shows the likelihood $100(1-\alpha)\%$ joint confidence regions, with a significance level of $\alpha = 5 \cdot 10^{-2}$. The results are shown for pairs of parameters $\boldsymbol{\beta}_\imath$ and $\forall \imath \in \{1,2,7,8\}$ described by sampling the parameter space, $\boldsymbol{\beta} \in \mathbb{R}^{N_\beta}$, with LHS. It is evident that the significant reduction in parameter correlation observed in 4a also improved the elliptical representation of the confidence regions, as discussed by Bates and Watts (1988). Moreover, it is noteworthy that the relative errors of the parameters ΔE^{eq}_1 and E^{fwd}_3 were independent of the reference temperatures adopted, Fig. 4b, and that the apparent reduction in the relative errors of these parameters were governed instead by the reduction in $\Phi(\hat{\boldsymbol{\beta}})$ (see Eq. (27)). This reduction occurred due to enhanced convergence of the LMA when the DOP (see Eq. (26)) was re-optimized with the optimal set of reference temperatures,

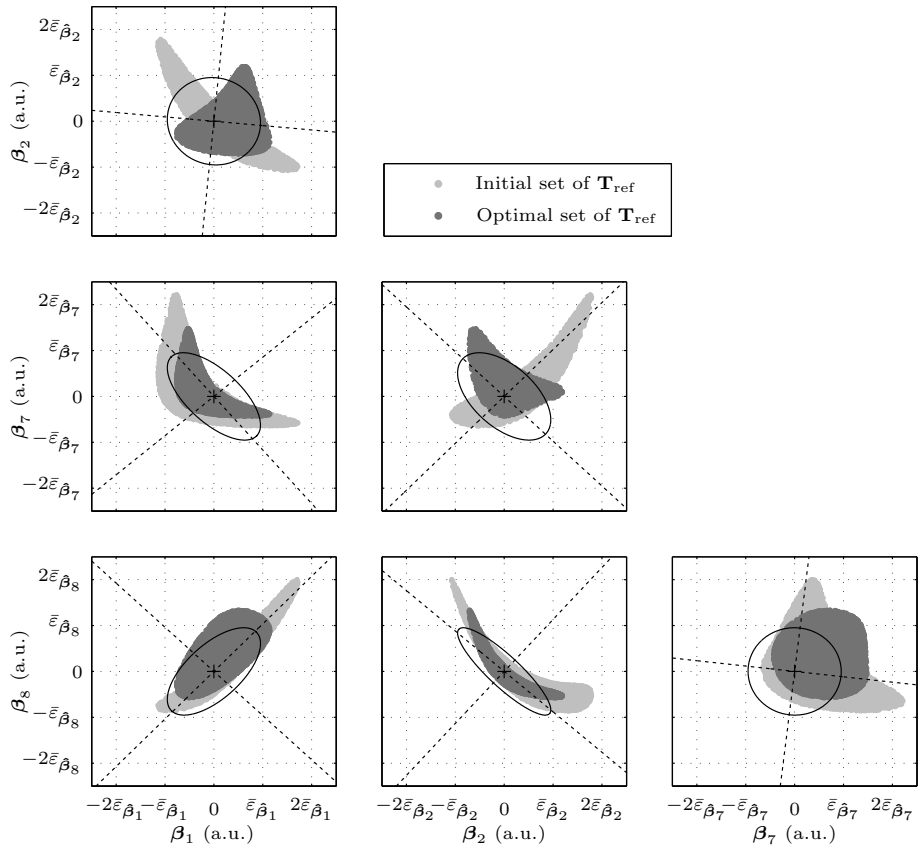

Figure 5: Nominal 95% likelihood confidence region (see Eq. (33)) for pairs of normalized and centered parameters $\boldsymbol{\beta}_\imath$ and $\forall \imath \in \{1, 2, 7, 8\}$. The $(-)$ symbol shows the approximate joint 95% confidence region, while $(+)$ shows the normalized and centered least-squares estimates, $\hat{\boldsymbol{\beta}}_\imath$. $(--)$ shows the principal axes given by the eigenvectors of $\boldsymbol{\Sigma}(\hat{\boldsymbol{\beta}}, \hat{\mathbf{T}}_{\text{ref}})$.

$\hat{\mathbf{T}}_{\text{ref}}$.

7.2. Accuracy and Reliability of the Predicted Model Response

The QCM trajectory for all $N_{\Delta t}$ cycles was fractionated with assigned t_0 at the start of the $Zn(C_2H_5)_2$ precursor pulse in Fig. 2, which is the most convenient representation when determining $\hat{\nu}$ from Eq. (3). When solving the DOP

(see Eq. (26)), however, t_0 was assigned to the center of the carrier gas purge that followed the H_2O precursor pulse, such that it was possible to simulate a smooth rectangular function, $\Pi_\alpha(t, \Delta t_\alpha)$, that was composed of superposed logistic functions. This procedure redistributed the standard deviations of each temporal sample, while the extracted quantities $\hat{\nu}$ and $d\Delta\hat{m}_q|_{\Delta t}(dN_{\Delta t})^{-1}$ listed in Table 1 remained constant. Additionally, the collocation method (see Section 6.1) used to compute the limit-cycle solution was solved for 50 finite elements in the experimental time horizon $[0, \Delta t_j]$ and $\forall j \in \{1, 2, \cdots, N_j\}$, with three Radau collocation points in each element. Section 7.3 presents a comparison between the limit-cycle solutions determined with the collocation method and those determined by the verification simulation (see Fig. 3).

Fig. 6 presents the accumulated mass per unit QCM sensor area, $\langle m_q \rangle$, (see Eq. (18)) for the least-squares estimates listed in Table 3 and the associated $100(1-\alpha)\%$ confidence bands, for a representative set of calibration experiments. The figure verifies the precision of the simulated model response. The graphic representation for the experimental calibration datasets $j \in \{3, 8, 9, 14, 10\}$ (corresponding to one set for each temperature studied in the range $T \in [100, 200]$ (°C) (see Table 1)) shows that the model output agrees well with the experimental data. The confidence bandwidth is moderately narrow and replicates the temporal dependency of the model response. Thus, the accuracy and predictability of the transient mass gain, $\langle m_q \rangle$, can be determined by analyzing the bandwidth and shape of the approximate confidence bands. The effect of the uncertainty on the precision of the parameter estimates can also be evaluated in this way. However, the poorest fit of $\langle m_q \rangle$ in the experimental time horizon occurred for the initial increase in mass at the leading edge of the $Zn(C_2H_5)_2$ precursor pulse. It is noteworthy that this temporal region was associated with the highest experimental uncertainty, and – since the variance $\sigma^2_{\langle \Delta\hat{m}_q \rangle}$ of each temporal sampling point is balanced in the time-variant weight matrix, $\mathbf{W}$ – the error that this set of sampling points contributed to the weighted sum of squared residuals (see Eq. (27)) was considerably reduced. Finally, it is also noteworthy that the increase in $\langle m_q \rangle$ shortly before the αth precursor pulse on-

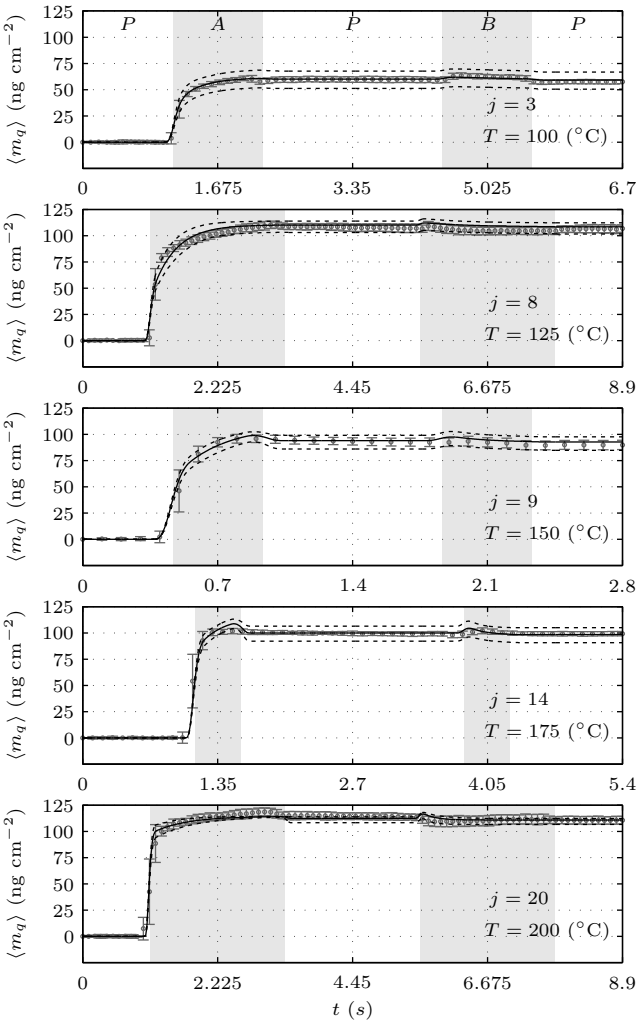

Figure 6: Transient mass gain per unit area of exposed surface of QCM sensor for a single-pulse sequence horizon $[0, \Delta t_j]$ and the calibration set $j \in \{3, 8, 9, 14, 10\}$ listed in Table 1. The $(-)$ symbol shows the integral mean value of the QCM mass gain, $\langle m_q \rangle$, (see Eq. 18), while $(--)$ shows the associated uncertainty bands for the expected response determined by the parameter bounds that were specified according to the 95% joint confidence region governed by Eq. (33). $(\circ)$ shows the *in situ* QCM mean mass gain, $\langle \Delta \hat{m}_q \rangle$, while the error bars show the associated confidence intervals, $\sigma_{\langle \Delta \hat{m}_q \rangle}$. The shaded rectangles indicate the precursor pulse interval endpoints.

set arises from the tailing of the smooth rectangular function, $\Pi_\alpha(t, \Delta t_\alpha)$, used to model the non-overlapping precursor injections.

The transient mass gain trajectory determined from Eq. (18) can be mechanistically interpreted by means of the chemical composition of the growth surface, i.e. the fractions of the surface that are covered by precursor adduct species, by adduct species in their transition state, and the chemisorbed species that are left by the ligand elimination reactions (see Reactions (R2 and R3)). Thus, the trajectory of the transient mass gain during the $Zn(C_2H_5)_2$ precursor exposure arises from the complex interdependence between the gas–surface precursor adsorption equilibrium (Reaction (R2a)), the adsorbed precursor adduct and transition state equilibrium (Reaction (R2b)), and the irreversible ligand elimination surface reaction (Reaction (R2c)). Specifically, the net contribution from Reaction (R2a) to Eq. (18) is the degree of saturation of the fractional surface coverage of hydroxyl groups, while the accumulated mass is unchanged as Reaction (R2b) proceeds. The contribution from Reaction (R2c), in contrast, arises from the production of $\langle\hat{\nu}\rangle$ C_2H_6 molecules, which subsequently desorb to the gas-phase.

Reversible chemisorbed surface species θ_κ and $\kappa \in \{B*, C*\}$ are desorbed in particular at the trailing edge of the $Zn(C_2H_5)_2$ precursor exposure, as $p_A \to 0$ in Eq. (21e), which can be seen most clearly for $j = \{9, 14\}$ in Fig. 6. Desorption is more pronounced at elevated temperatures, since the reaction rate coefficient k_2^{rev} in Eq. (22a) is higher. The $\langle m_q\rangle$ trajectory is approximately constant during the subsequent carrier gas purge, which implies that negligible desorption takes place, and thus reversible chemisorbed species are desorbed almost instantaneously as $p_A \to 0$ at the trailing edge of the precursor exposure. However, it is noteworthy that the DAE system (see Eq. (21)) that governs the fractional surface coverage species dynamics for Reactions (R2 and R3) can reproduce desorption phenomena during the entire carrier gas purge period, as long as the surface species $\kappa \in \{B*, C*\}$ are present at the growth surface.

Furthermore, the physicochemical phenomena that govern the appearance of the $\langle m_q\rangle$ trajectory during the subsequent H_2O precursor exposure are anal-

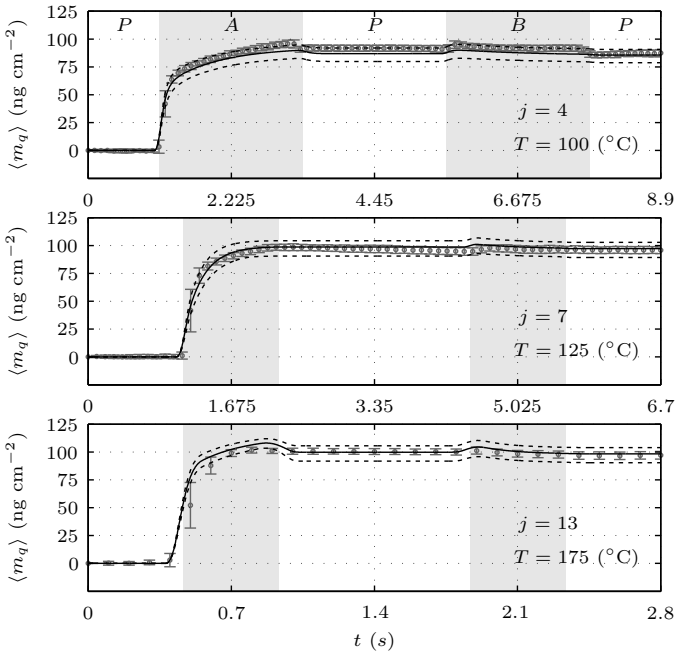

Figure 7: Transient mass gain per unit exposed surface QCM sensor area for a single-pulse sequence horizon $[0, \Delta t_j]$ and the validation set $j \in \{4, 7, 13\}$ listed in Table 1. The $(-)$ symbol shows the integral mean value of the QCM mass gain, $\langle m_q \rangle$, (see Eq. 18), while $(--)$ shows the associated uncertainty bands for the expected response determined by the parameter bounds that were specified according to the 95% joint confidence region governed by Eq. (33). $(\circ)$ shows the *in situ* QCM mean mass gain, $\langle \Delta \hat{m}_q \rangle$, while the error bars show the associated confidence intervals, $\sigma_{\langle \Delta \hat{m}_q \rangle}$. The shaded rectangles indicate the precursor pulse interval endpoints.

ogous to those of the $Zn(C_2H_5)_2$ precursor exposure, although the molecular masses of the reagents differ. Hence, the mass increases at the leading edge of the H_2O pulse, which arises from the adsorption and formation of the precursor adduct species and its transition state ($\kappa \in \{E*, F*\}$). The increase in mass takes place before the ligand elimination reaction (Reaction (R3c)) converts the transition states $F*$, and before they have passed through the reverse reaction (Reaction R3b) to their corresponding adduct state $E*$ (and subsequently desorbed from the growth surface by means of Reaction (R3a)). The increase in

mass is most pronounced at low temperatures (as for $j = 3$ in Fig. 6) and which arises from the aforementioned temperature dependence of the elementary surface reaction kinetics. However, the difference in molecular mass between the initial and terminal surface species in Reaction (R3), denoted ΔM_B in Eq. (3), means that the net contribution to Eq. (18) from this half-reaction is less than zero for values of $\nu < 2 - M_{\mathrm{H_2O}}(M_{\mathrm{C_2H_6}})^{-1} \approx 1.40$. Obviously, this is the case for the $\langle \hat{\nu} \rangle$ determined in Section 2.4.

The ultimate test of the model is to compare it with the validation set. The region of validity is the union between the calibration region and the region covered by the validation experiments (Brereton, 2003). Fig. 7 shows the model response for the experimental validation dataset with $j \in \{4, 7, 13\}$ (see Table 1). The trajectory of the transient mass gain, $\langle m_q \rangle$, shows that the performance of the model is satisfactory, with narrow confidence bands and conformal growth per limit cycle, $d\langle m_q \rangle|_{\Delta t}(dN_{\Delta t})^{-1}$. The predictions of the model are assessed in more detail below to determine the impact of the precursor pulse duration and deposition temperature on film growth per limit cycle, and to distinguish between ALD in saturating and in non-saturating film growth conditions.

7.2.1. Effect of Deposition Temperature on Film Growth per Limit Cycle

Fig. 8 shows the model predicted and experimentally observed effects of deposition temperature, T, on the film growth rate per limit cycle. Non-saturating growth is obtained for the precursor exposure period $\widetilde{\Delta t}_\alpha = 0.40$ (s) in the entire temperature range $[75, 275]$ (°C). Additionally, the rate of film growth per limit cycle does not show a self-limiting growth region under these conditions, as $d\langle m_q \rangle|_{\Delta t}(dN_{\Delta t})^{-1}$ falls significantly for $T < 175$ (°C) and for $T > 175$ (°C). The initially low MGPC values in the low-temperature region ($T < 175$ (°C)) arises from the activation barrier of the forward elementary reactions $i \in \{2, 3, 5, 6\}$ (see Reactions (R2 and R3)) which make it thermodynamically more favorable for adsorbed precursors to desorb than to proceed through the surface ligand-elimination reactions. The activation energies of these reactions are more easily overcome as the temperature increases, which promotes the equi-

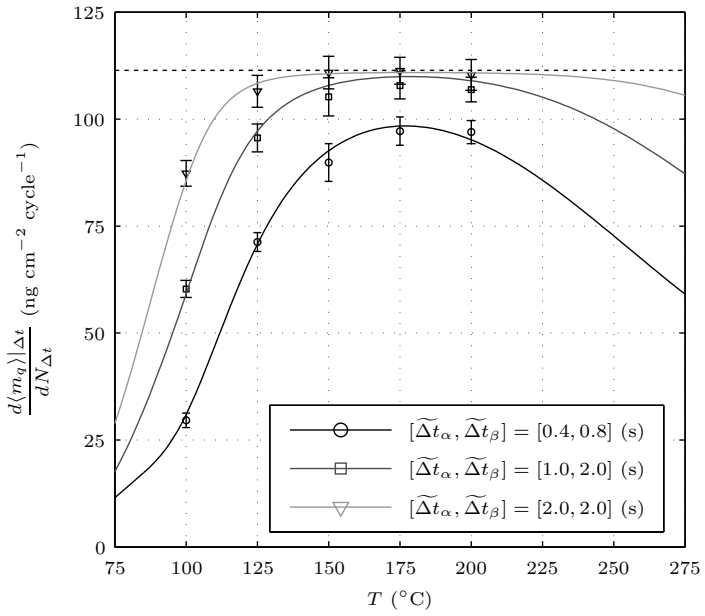

Figure 8: The effect of deposition temperature in the range $T \in [75, 275]$ (°C) on the mass gain per limit cycle, $d\langle m_q\rangle|_{\Delta t}(dN_{\Delta t})^{-1}$, at three levels of precursor exposure in the range $\widetilde{\Delta t}_\alpha \in [0.4, 2.0]$ (s) with $\alpha \in \{A, B\}$. The symbols $(\circ, \square, \triangledown)$ show the estimated MGPC, $d\Delta\hat{m}_q|_{\Delta t}(dN_{\Delta t})^{-1}$, scaled with the *ex situ* XRR reference thickness, while the error bars show the associated confidence intervals, $\sigma_{\frac{d\Delta\hat{m}_q|_{\Delta t}}{dN_{\Delta t}}}$, for the dataset $j \notin \{2, 6, 10, 14, 18\}$ in Table 1. $(--)$ shows the maximum MGPC, max $d\Delta\hat{m}_q|_{\Delta t}(dN_{\Delta t})^{-1}$.

librium surface coverage of intermediate complexes and, ultimately, the concentration of surface species onto which the precursors can adsorb and cause in this way the increase in growth rate.

In contrast, the activation energy of the reversed elementary reactions $i \in \{2, 5\}$ is overcome in the high temperature region ($T > 175$ (°C)) under these non-saturating conditions, which makes desorption more favorable. This lowers the rate of conversion of the fractional surface coverage of $\kappa \in \{A*, D*\}$ per limit cycle. This implies that the significant increase in the reaction rate coefficients k_2^{rev} and k_5^{rev} (see Eqs. (22a and 22b)), governs to a high extent the overall MGPC at elevated temperatures. Additionally, it is noteworthy that the gas–

surface equilibrium reactions $i \in \{1, 4\}$ also proceed faster in both directions (see Eqs. (21e and 21f)).

Fig. 8 shows that MGPC approaches the maximum growth per limit cycle for the precursor exposure period $\widetilde{\Delta t}_\alpha = 1.0$ (s). This corresponds to surface saturation and is associated with the maximum surface concentrations, Λ, (see Section 2.4). The observed flat profile that encloses the maximum deposition rate indicates that a self-limiting growth region appears progressively under these conditions. As expected, this ideal self-limiting growth region widens for longer periods of precursor exposure, while it remains limited by the aforementioned thermodynamics of the precursor half-cycle reactions at low and high temperatures.

7.2.2. Effect of Precursor Exposure Duration on Film Growth per Limit Cycle

Fig. 9 shows the effect of precursor pulse duration, Δt_α and $\alpha \in \{A, B\}$, on the film growth rate per limit cycle, $d\langle m_q \rangle|_{\Delta t}(dN_{\Delta t})^{-1}$. The exposure periods of the two precursors were set to be equal and to vary in parallel in the range $\Delta t_\alpha \in (0, 5]$ (s), while the carrier gas purge period was maintained at $\Delta t_\beta := 2\Delta t_\alpha$ (s). It is evident that $d\langle m_q \rangle|_{\Delta t}(dN_{\Delta t})^{-1}$ approaches the limiting value corresponding to surface saturation asymptotically, as expected for the self-terminating ALD reaction kinetics. This behavior is independent of the deposition temperature. Figs. 8 and 9 make it also clear that the model predictions agree well with the experimental data, and successfully distinguish growth per limit cycle between saturating and non-saturating conditions. The predictive power of the model is crucial in this context, especially since it is necessary to keep the individual precursor doses to a minimum while maintaining sufficiently high exposure, at the lower bound defined by non-saturating conditions (Travis and Adomaitis, 2013b), in order to optimize commercial reactor systems. This is even more critical in the high-throughput spatial ALD systems that are under development for use in roll-to-roll and other large-substrate applications.

Finally, it is important to note that $d\langle m_q \rangle|_{\Delta t}(dN_{\Delta t})^{-1}$ is ultimately governed by the half-cycle average exposure dose, $\langle \delta_\alpha \rangle$, for the αth precursor. The

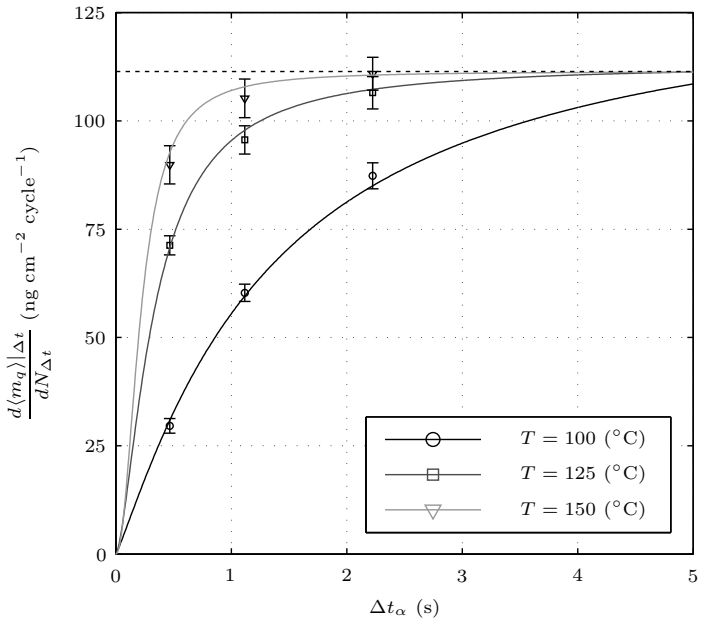

Figure 9: The effect of precursor pulse duration, Δt_α and $\forall \alpha \in \{A, B\}$ set to be equal and to vary in parallel in the range $\Delta t_\alpha \in (0.0, 5.0]$ (s), on the mass gain per limit cycle, $d\langle m_q\rangle|_{\Delta t}(dN_{\Delta t})^{-1}$, sampled at $T \in \{100, 125, 150\}$ (°C) and with $\Delta t_\beta := 2\Delta t_\alpha$. The symbols $(\circ, \square, \triangledown)$ show the estimated MGPC, $d\Delta\hat{m}_q|_{\Delta t}(dN_{\Delta t})^{-1}$, scaled with the *ex situ* XRR reference thickness, while the error bars show the associated confidence intervals, $\sigma_{\frac{d\Delta\hat{m}_q|_{\Delta t}}{dN_{\Delta t}}}$, for the dataset $j \in \{1, 3, 4, 5, 7, 8, 9, 11, 12\}$ in Table 1. $(--)$ shows the maximum MGPC, max $d\Delta\hat{m}_q|_{\Delta t}(dN_{\Delta t})^{-1}$.

exposure of the growth surface is characterized by the time-dependent, local, precursor partial pressure during the exposure period and during a portion of each purge period:

$$\langle \delta_\alpha \rangle = \frac{1}{(\zeta_{\text{end}} - \zeta_0)} \int_{t_0}^{t_f} \int_{\zeta_0}^{\zeta_{\text{end}}} p_\alpha d\zeta dt \tag{34}$$

in which $t_f = \Delta t_\alpha + \Delta t_\beta$. Thus, it is expected that an increase in the precursor mass flow, $\dot{Q}_\alpha$, will yield a higher partial pressure, p_α, and consequently enhance the deposition rate, $d\langle m_q\rangle|_{\Delta t}(dN_{\Delta t})^{-1}$. This will achieve saturation growth conditions at exposure times, Δt_α, that are lower than those presented Fig. 9.

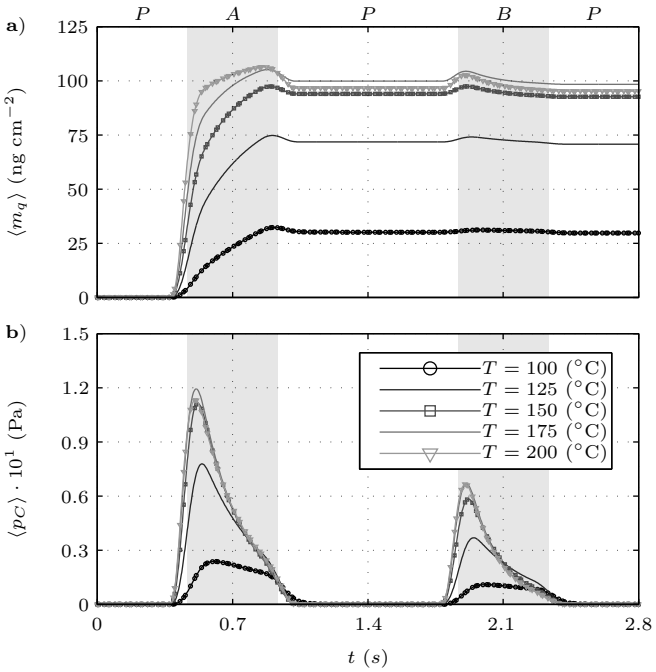

Figure 10: Model-generated transient mass gain per unit of exposed QCM sensor area, $\langle m_q \rangle$, and the spatial integral mean value of p_C in $z \in [z_0, z_{\text{end}}]$ (m), resolved at a single pulse sequence $[\widetilde{\Delta t}_\alpha, \widetilde{\Delta t}_\beta] = [0.4, 0.8]$ (s) in the temperature range $T \in [100, 200]$ (°C). $(\circ, \square, \triangledown)$ show the collocation based trajectories at the Radau collocation point locations, while $(-)$ shows the simulated trajectories. The shaded rectangles indicate the precursor pulse interval endpoints.

An extensive investigation of the precursor exposure dose is beyond the scope of the present study, and the reader is referred to Holmqvist et al. (2013a,b), for example, for more details.

7.3. Time Evolution of the Stable Limit-Cycle Solutions

This section describes several aspects of the dynamic ALD limit-cycle solution. The limit-cycle solutions shown in Figs. 10–13 present the same case study with an assigned pulse sequence $[\widetilde{\Delta t}_\alpha, \widetilde{\Delta t}_\beta] = [0.4, 0.8]$ (s) and temperature range $T \in [100, 200]$ (°C). This corresponds to the operating conditions of the experimental datasets $j \in \{1, 5, 9, 13, 17\}$ listed in Table 1. Figs. 10–

13 present also the results from the collocation method, and the figures thus compare these results with those obtained from the model integration of the DAE system with the CVODES solver (see Fig. 3). The results are practically identical. The collocation method used corresponds to a Radau solver with a fixed step size, while the solver used in the verification simulation uses a variable step size formula with backward differentiation and error control. Thus, the solution found by the CVODES solver fulfils the model equations, at least to the specified tolerances.

Fig. 10a confirms the mechanistic interpretation presented in Section 7.2, in that the slope of the trajectory of mass gain, $\langle m_q \rangle$, generated by the model at the leading edges of both precursor exposure periods becomes steeper as the temperature increases. Moreover, the elementary precursor adduct desorption reactions, $i \in \{2, 5\}$, and the precursor gas–surface equilibrium reactions, $i \in \{1, 4\}$, proceed faster in the high-temperature region, and these reactions thus demonstrate more pronounced desorption effects. They ultimately govern the overall decrease in mass gain per limit cycle. It is noteworthy that the terminal value of the mass gain trajectory, $\langle m_q \rangle(t_f)$, for $T = 200$ (°C) falls below that of $T = 175$ (°C) (which can be compared with the temperature dependence of $d\langle m_q \rangle|_{\Delta t}(dN_{\Delta t})^{-1}$ in Fig. 8).

Fig. 10b shows a complementary method for analyzing the dynamics of Reactions (R2 and R3). This method considers the trajectory of the integral mean value of the gas-phase composition of C_2H_6 on the spatial domain, $z \in [z_0, z_{\text{end}}]$. This is the most convenient method for elucidating the ligand-elimination reactions, $i \in \{3, 6\}$, since the production of C_2H_6 is governed exclusively by the continuation of these irreversible reactions. This method enables the number of hydroxyl groups that react with each $Zn(C_2H_5)_2$ precursor molecule, ν, to be estimated by temporal and spatial integration of the reaction byproduct that is released during the $Zn(C_2H_5)_2$ precursor half-reaction $[t_0, t_1]$ and the entire

time horizon, $[t_0, t_f]$. The number of hydroxyl groups is thus given by:

$$\nu = \nu_L \int_{t_0}^{t_1} \int_{z_0}^{z_{\text{end}}} p_C dz dt \left(\int_{t_0}^{t_f} \int_{z_0}^{z_{\text{end}}} p_C dz dt \right)^{-1} \tag{35}$$

in which ν_L is the total number of ligands of the adsorptive organometallic precursor, and $t_1 = \Delta t_A + \Delta t_P$ is the upper limit for the nominator temporal integral. Finally, it is noteworthy that the values determined from Eq. (35) and the $\langle p_C \rangle$ trajectories depicted in Fig. 10b, correspond to the value of $\langle \hat{\nu} \rangle$ estimated from Eq. (3) and the *in situ* QCM mean mass gain, $\langle \Delta \hat{m}_q \rangle$ (see Section 2.4).

Computing the limit-cycle solution over the time horizon $[t_0, t_f]$ requires that the terminal composition of the fractional surface coverage species, $\theta_\kappa(t_f)$ and $\forall \kappa \in \{A*, \cdots, F*\}$, returns to its initial composition, $\theta_\kappa(t_0)$, (see Eq. (24a)). The forced-period system dynamics are described by the DAE system in Eq. (25), which is subject to the surface state initial conditions (see Eq. (25b)) and terminal constraints (see Eq. (25c)). This implies that an unambiguous method to numerically compute limit-cycle ALD dynamic solutions is essential for the accuracy, reliability and reproducibility of the solution of such DAE systems. Fig. 11 presents a representative limit-cycle solution computed using the collocation method (see Section 6.1), where the fractional surface state composition is depicted as a function of time over the entire horizon $[t_0, t_f]$. Under these conditions, the growth surface approaches a fully saturated state during both of the precursor exposures. The surface state limit-cycle dynamic model (see Eq. (21)) states that saturating ALD conditions per limit-cycle are obtained if the fractional surface coverage $\theta_{A*}(t_0) = \theta_{A*}(t_f) := 1.0$, and consequently $\theta_\kappa(t_0) = \theta_\kappa(t_f) := 0.0$ and $\forall \kappa \notin A*$, according to Eq. (24b). Thus, an important consequence of the limit-cycle solutions depicted in Fig. 11 is that they enable to mechanistically quantify the difference between the saturating ALD and non-saturating film growth conditions previously observed in Figs. 8 and 9 by means of the underlying surface-state limit-cycle dynamics.

Fig. 11 shows that $\theta_{A*} \to 0$ during the $Zn(C_2H_5)_2$ exposure as the growth

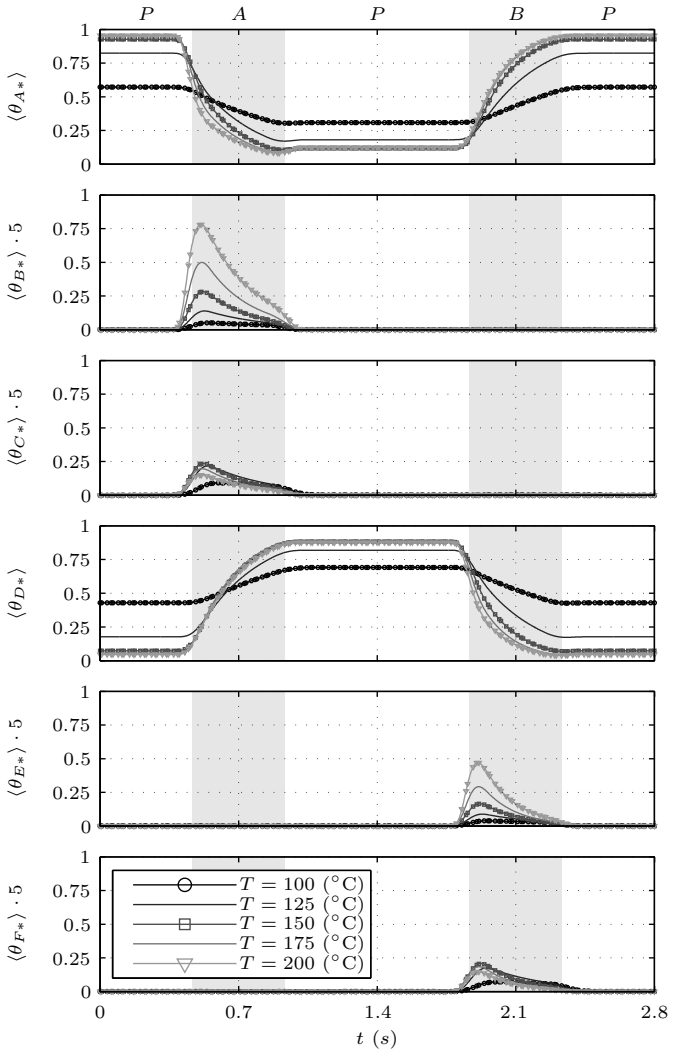

Figure 11: Projection of the fractional surface coverage limit-cycle dynamics sampled in the temperature range $T \in [100, 200]$ (°C) with the pulse sequence $[\widetilde{\Delta}t_\alpha, \widetilde{\Delta}t_\beta] = [0.4, 0.8]$ (s). The symbol $(-)$ shows the simulated integral mean value of $\langle\theta_\kappa\rangle$ and $\kappa \in \{A*, B*, C*, D*\}$ in $\zeta \in [\zeta_0, \zeta_{\text{end}}]$ (m), while the corresponding solutions from the collocation method at the Radau collocation point locations are shown by $(\circ)$ for $T = 100$ (°C), $(\square)$ for $T = 150$ (°C), and $(\triangledown)$ for $T = 200$ (°C). The shaded rectangles indicate the precursor pulse interval endpoints.

surface saturates with the precursor adduct, $B*$, through Reaction (R2a), and the precursor adduct in its transition state, $C*$, through Reaction (R2b). The adduct in the transition state is also subject to the ligand-elimination reaction (Reaction (R2c)), which governs the formation of $D*$ onto which the H_2O precursor can adsorb. The H_2O half-reaction (see Reaction (R3)) can subsequently proceed in an analogous manner, ultimately resulting in the reformation of $A*$ through Reaction (R3c). Fig. 11 also shows that the fractional surface coverages of adduct species, $\kappa \in \{B*, E*\}$, and the corresponding adducts in their transition states, $\kappa \in \{C*, F*\}$, are approximately five to ten times smaller than the coverages of the permanently bound species, $\kappa \in \{A*, D*\}$. It is important to determine the intermediate surface state coverage of these species since they are very difficult to detect experimentally, as surface state measurements correspond to permanently bound species (Travis and Adomaitis, 2013b).

Figs. 12 and 13 present alternative views of the fractional surface coverage limit-cycle dynamics associated with the $Zn(C_2H_5)_2$ half-reaction (Reaction (R2)) and the H_2O half-reaction (see Reaction (R3)), respectively. The limit-cycle solutions can be easily identified in the phase plane portraits, and it is evident that the projected surface state trajectories depicted in Fig. 11 are closed curves, which means that all states conform to periodic boundary conditions over the time horizon $[t_0, t_f]$. The closed trajectories show the evolution of the fractional surface coverage with time, with a counter-clockwise direction of motion (i.e. the direction of increasing time) from the initial composition in Fig. 11. It is noteworthy, that the closed curves for $\langle\theta_\kappa\rangle$ shown in Figs. 11–13 are spatial averages over the domain $\zeta \in [\zeta_0, \zeta_{\text{end}}]$ (see Figure 1b), in order to make the figures clear. However, it must be remembered that Eq. (16) is a PDE, spatially discretized with FVM elements (see Section 4.5), which implies that $N_{\text{FVM}} \times N_\kappa$ limit-cycles appear throughout the entire spatial domain $z \in [z_0, z_{\text{end}}]$. Consequently, $N_{\text{FVM}} \times (N_\kappa - 1)$ terminal constraints (see Eq. (24)) must also be fulfilled. Finally, Figs. 10–13 reveal rigorous limit-cycle dynamics for both the gas-phase and surface state species, and for the ALD film growth. These dynamics are essential for process analysis, design and optimization.

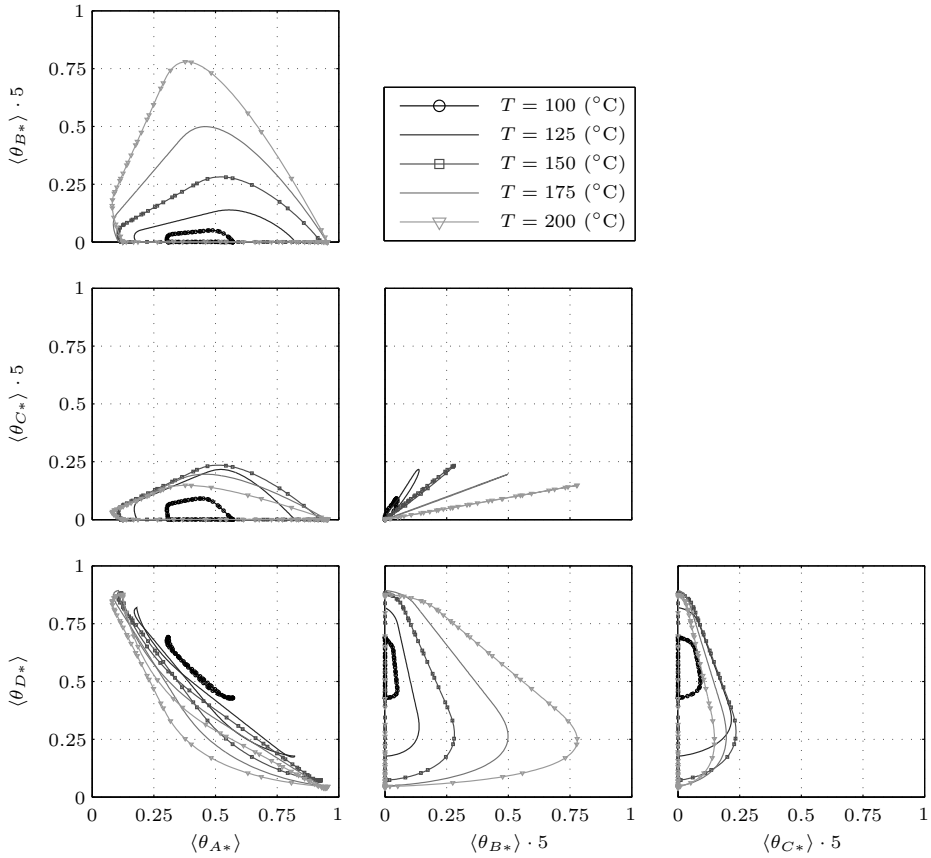

Figure 12: Phase plane portrait of the fractional surface coverage limit-cycle dynamics relevant to the $Zn(C_2H_5)_2$ precursor ALD half-reaction (Reaction (R2)) in the temperature range $T \in [100, 200]$ (°C). $(-)$ shows the simulated integral mean value of $\langle\theta_\kappa\rangle$ and $\kappa \in \{A*, B*, C*, D*\}$ in $\zeta \in [\zeta_0, \zeta_{\text{end}}]$ (m), while the corresponding solutions from the collocation method at the Radau collocation point locations are shown by $(\circ)$ for $T = 100$ (°C), $(\square)$ for $T = 150$ (°C), and $(\triangledown)$ for $T = 200$ (°C).

8. Concluding Remarks

In this paper, a novel physically based model of a viscous continuous cross-flow ALD reactor with temporally separated precursor pulsing was developed and applied to ZnO ALD with $Zn(C_2H_5)_2$ and H_2O precursors. Model components that describe reactor-scale gas-phase dynamics and surface state dynamics

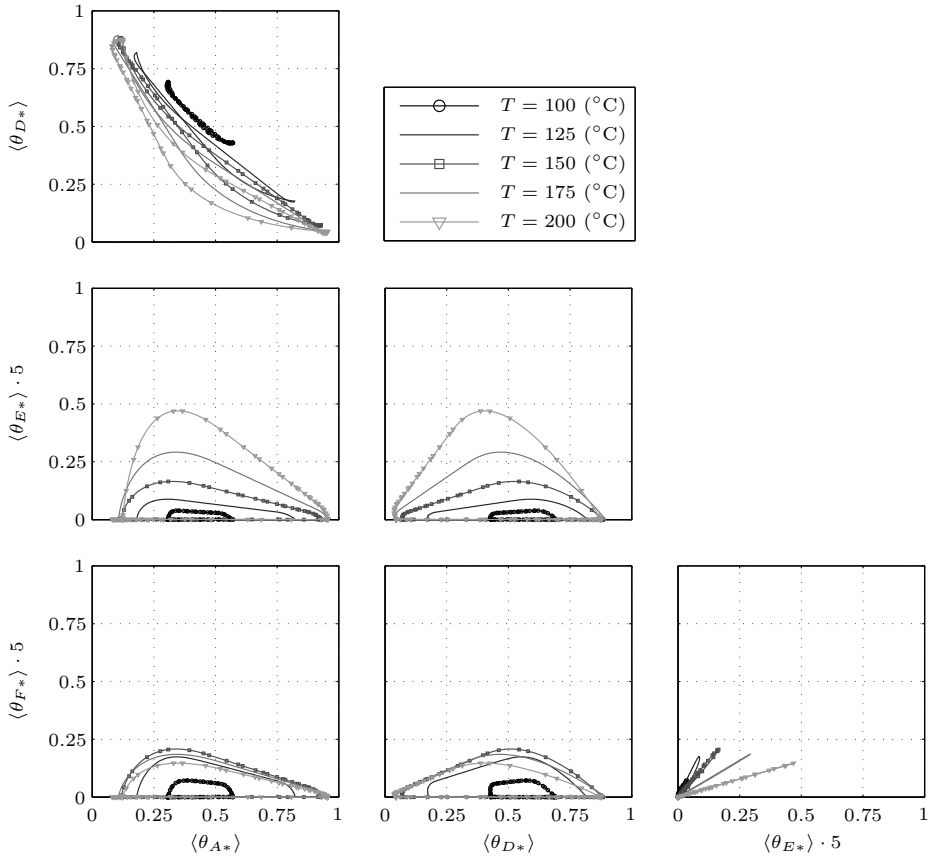

Figure 13: Phase plane portrait of the fractional surface coverage limit-cycle dynamics relevant to the H_2O precursor ALD half-reaction (Reaction (R3)) in the temperature range $T \in [100, 200]$ (°C). $(-)$ shows the simulated integral mean value of $\langle\theta_\kappa\rangle$ and $\kappa \in \{A*, D*, E*, F*\}$ in $\zeta \in [\zeta_0, \zeta_{\text{end}}]$ (m), while the corresponding solutions from the collocation method at the Radau collocation point locations are shown by $(\circ)$ for $T = 100$ (°C), $(\square)$ for $T = 150$ (°C), and $(\triangledown)$ for $T = 200$ (°C).

have been integrated to accurately characterize the continuous, cyclic ALD reactor operation that is described by limit-cycle dynamic solutions. The steady cyclic operation was discretized using a Radau collocation scheme in time and solved using the CasADi interface to IPOPT. The surface-reaction model, which accounts for the temporal evolution of the growth surface composition, is gov-

erned by the reaction rate expressions of the trapping-mediated mechanism, in which it is assumed that both precursors follow structurally similar reaction sequences. These sequences are initiated by the formation of adsorption and precursor adducts, which is followed by an adduct/transition-state equilibrium reaction that is terminated with an irreversible reaction in which ligands are eliminated.

The work described in this paper was motivated by the predictive capabilities of physically based ALD process models, as such models can be used in the design of novel reactors and in the optimization of deposition conditions. For this reason, a comprehensive study of *in situ* growth kinetics with QCM diagnostics was carried out. This provided quantitative submonolayer resolution of the mass gain that occurs during a single ALD pulse sequence, from which the Arrhenius kinetic parameters involved in the ALD reaction intrinsic kinetic mechanism were estimated using a general dynamic optimization problem.

The assessment of the accuracy and reliability of the parameter estimates reported here, showed that the parameters are highly correlated, as expected. These correlations arise from the complex interdependence between elementary surface reactions involved in ALD and the intrinsic mathematical structure of the Arrhenius equation, and could be reduced through optimal reparameterization of the Arrhenius equation by means of the anti-correlation procedure described by Schwaab et al. (2008). This improved the precision of the parameter estimates. Predictions from the model of the transient mass gain per unit area of exposed surface QCM sensor (resolved for a single pulse sequence) agree well with both calibration data and validation data, under a wide range of operating conditions. The predictions are associated with narrow confidence bands. The model also predicts accurately the impacts of the precursor pulse duration and of the deposition temperature on the film growth per limit cycle, and can in this way distinguish between ALD in saturating and in non-saturating film growth conditions.

The principal contribution of this paper is the rigorous transport/reaction model that is based on PDAEs and the continuous reactor operation described

by limit-cycle solutions that are unambiguous for several applications. Another important contribution is the dynamic procedure used to estimate parameters from *in situ* experimental data in order to identify accurately kinetic data and to develop novel ALD reaction intrinsic kinetic mechanisms. The fundamental understanding of the ALD process that was obtained by analyzing the limit-cycle dynamics for both the gas-phase and surface state species, and by analyzing the ALD film growth, is of practical interest when scaling ALD processes to large-surface-area substrates and high-throughput production.

Acknowledgement

The authors acknowledge the supported by the Swedish Research Council under Grant no. 2006-3738. Fredrik Magnusson is a member of the LCCC Linnaeus Center and the eLLIIT Excellence Center at Lund University.

Nomenclature

Roman letters

A'	cross section area of the reaction chamber	m^2
A_i	frequency factor in the Arrhenius equation	$(\mathrm{mol\,m^{-2}})^{1-n_i}\,\mathrm{Pa^{-1}\,s^{-1}}$, $(\mathrm{mol\,m^{-2}})^{1-n_i}\,\mathrm{s^{-1}}$
$\mathbf{C}$	$(N_\beta \times N_\beta)$ parameter correlation matrix	–
$\mathscr{D}_{\alpha\beta}$	binary diffusivity	$\mathrm{m^2\,s^{-1}}$
E_i	activation energy	$\mathrm{J\,mol^{-1}}$
$\mathbf{F}$	system of differential algebraic equations	–
$F_{(N_\beta,\varphi;\alpha)}$	Fisher's F-distribution	–
$\mathbf{g}$	response function	–
$\mathbf{J}$	parameter Jacobian matrix	–
k_i	reaction rate constant	$(\mathrm{mol\,m^{-2}})^{1-n_i}\,\mathrm{Pa^{-1}\,s^{-1}}$, $(\mathrm{mol\,m^{-2}})^{1-n_i}\,\mathrm{s^{-1}}$
M_α	molar mass	$\mathrm{kg\,mol^{-1}}$
m_s	film mass increment	$\mathrm{kg\,m^{-2}}$
n_i	surface reaction order	–
p	pressure	Pa
$\dot{Q}_\alpha$	volumetric flow rate at STP	$\mathrm{Nm^3s^{-1}}$
R	universal gas constant	$\mathrm{J\,mol^{-1}\,K^{-1}}$
r_i	surface reaction rate	$\mathrm{mol\,m^{-2}\,s^{-1}}$
S_α	source term in the general transport equation	$\mathrm{kg\,m^{-3}\,s^{-1}}$
s^2	variance estimate of σ^2	–
T	temperature	K
t	time	s
$t_{(\varphi;\alpha/2)}$	Student's t-distribution	–
$\mathbf{u}$	design variables	–
v_z	linear velocity	$\mathrm{m\,s^{-1}}$
$\mathbf{W}$	weight matrix	–
$\mathbf{w}$	algebraic variables	–
$\mathbf{x}$	state variables	–
$\mathbf{y}$	measured state variables	–
z	spatial coordinate	m

Greek letters

α	significance level	–
$\boldsymbol{\beta}$	calibration parameter vector	–
Δt_α	pulse duration	s
δ_α	half-cycle average precursor dose	Langmuir
$\varepsilon_{\hat{\beta}_\imath}$	normalized margin of error	–
ζ	QCM local coordinate variable	m
θ_κ	fractional surface coverage of surface species	–
Λ	maximum molar concentration of surface sites	$\mathrm{mol\,m^{-2}}$
μ	dynamic viscosity of the gas mixture	$\mathrm{kg\,m^{-1}\,s^{-1}}$
ν	numbers of surface OH groups reacting	
	with each $Zn(C_2H_5)_2$	–
ξ_i	surface reaction stoichiometric coefficient	–
ρ	density of the gas mixture	$\mathrm{kg\,m^{-3}}$
$\boldsymbol{\Sigma}$	parameter covariance matrix	–
Φ	weighted sum of squared residuals	$\mathrm{ng\,cm^{-2}}$
Π_α	characteristic function of t and Δt_α	–
φ	degrees of freedom	–
ω_α	mass fraction of gaseous species	–

Subscripts and superscripts

0	initial value
α, β	gaseous species indices
i	surface reaction index
$\imath$	calibration parameter index
j	calibration and validation set index
κ	surface species index
q	quartz crystal
STP	state variable at STP
s	solid
ref	state at the reference temperature

References

Aarik, J., Aidla, A., Jaek, A., Leskelä, M., Niinisto, L., 1994a. In situ study of a strontium β-diketonate precursor for thin-film growth by atomic layer epitaxy. Journal of Materials Chemistry 4, 1239–1244.

Aarik, J., Aidla, A., Kasikov, A., Mändar, H., Rammula, R., Sammelselg, V., 2006. Influence of carrier gas pressure and flow rate on atomic layer deposition of HfO_2 and ZrO_2 thin films. Applied Surface Science 252 (16), 5723–5734.

Aarik, J., Aidla, A., Kukli, K., 1994b. In situ characterization of ALE growth by reagent pulse delay times in a flow-type reactor. Applied Surface Science 75 (1-4), 180–184.

Aarik, J., Aidla, A., Mändar, H., Uustare, T., 2001. Atomic layer deposition of titanium dioxide from $TiCl_4$ and H_2O: investigation of growth mechanism. Applied Surface Science 172 (12), 148–158.

Aarik, J., Siimon, H., 1994. Characterization of adsorption in flow type atomic layer epitaxy reactor. Applied Surface Science 81 (3), 281–287.

Adomaitis, R. A., 2010. Development of a multiscale model for an atomic layer deposition process. Journal of Crystal Growth 312 (8), 1449–1452.

Åkesson, J., 2008. Optimica—An extension of Modelica supporting dynamic optimization. In: 6th International Modelica Conference 2008. Modelica Association.

Åkesson, J., Årzén, K.-E., Gäfvert, M., Bergdahl, T., Tummescheit, H., 2010. Modeling and optimization with Optimica and JModelica.org—Languages and tools for solving large-scale dynamic optimization problems. Computers & Chemical Engineering 34 (11), 1737–1749.

Alam, M. A., Green, M. L., 2003. Mathematical description of atomic layer deposition and its application to the nucleation and growth of HfO_2 gate dielectric layers. Journal of Applied Physics 94 (5), 3403–3413.

997 Andersson, J., Åkesson, J., Diehl, M., 2012a. CasADi: A Symbolic Package
998 for Automatic Differentiation and Optimal Control. In: Forth, S., Hovland,
999 P., Phipps, E., Utke, J., Walther, A. (Eds.), Recent Advances in Algorith-
1000 mic Differentiation. Vol. 87 of Lecture Notes in Computational Science and
1001 Engineering. Springer Berlin Heidelberg, pp. 297–307.

1002 Andersson, N., Larsson, P.-O., Åkesson, J., Skålén, S., Carlsson, N., Nilsson, B.,
1003 2012b. Parameter Estimation of Dynamic Grade Transitions in a Polyethylene
1004 Plant. In: Proceedings of the 22nd European Symposium on Computer Aided
1005 Process Engineering. Elsevier B.V., London, pp. 1–5.

1006 Bakke, J. R., Pickrahn, K. L., Brennan, T. P., Bent, S. F., 2011. Nanoengineer-
1007 ing and interfacial engineering of photovoltaics by atomic layer deposition.
1008 Nanoscale 3, 3482–3508.

1009 Bard, Y., 1974. Nonlinear parameter estimation. Academic Press, New York.

1010 Bates, D. M., Watts, D. G., 1988. Nonlinear Regression Analysis and Its Appli-
1011 cations. John Wiley & Sons, Inc., New York.

1012 Baunemann, A., 2006. Precursor chemistry of Tantalum and Niobium nitride
1013 for MOCVD and ALD applications. Ph.D. thesis, Ruhr-University, Bochum.

1014 Biegler, L. T., 2010. Nonlinear Programming: Concepts, Algorithms, and Ap-
1015 plications to Chemical Processes. Society for Industrial Mathematics, PA,
1016 USA.

1017 Biegler, L. T., Cervantes, A. M., Wächter, A., 2002. Advances in simultaneous
1018 strategies for dynamic process optimization. Chemical Engineering Science
1019 57 (4), 575–593.

1020 Bird, R. B., Stewart, W. E., Lightfoot, E. N., 1960. Transport Phenomena, 2nd
1021 Edition. John Wiley & Sons, Inc., New York.

1022 Brereton, R. G., 2003. Chemometrics, Data Analysis for the Laboratory and
1023 Chemical Plant, 1st Edition. John Wiley & Sons, Inc., Chichester.

Carcia, P. F., McLean, R. S., Groner, M. D., Dameron, A. A., George, S. M., 2009. Gas diffusion ultrabarriers on polymer substrates using Al_2O_3 atomic layer deposition and sin plasma-enhanced chemical vapor deposition. Journal of Applied Physics 106 (2), 023533.

Cleveland, E. R., Henn-Lecordier, L., Rubloff, G. W., 2012. Role of surface intermediates in enhanced, uniform growth rates of TiO_2 atomic layer deposition thin films using titanium tetraisopropoxide and ozone. Journal of Vacuum Science & Technology A 30 (1), 01A150.

Davis, M. E., 1984. Numerical Methods and Modeling for Chemical Engineers, 1st Edition. John Wiley & Sons, Inc., New York.

Deminsky, M., Knizhnik, A., Belov, I., Umanskii, S., Rykova, E., Bagatur'yants, A., et al., 2004. Mechanism and kinetics of thin zirconium and hafnium oxide film growth in an ALD reactor. Surface Science 549 (1), 67–86.

Dillon, A. C., Ott, A. W., Way, J. D., George, S. M., 1995. Surface chemistry of Al_2O_3 deposition using $Al(CH_3)_3$ and H_2O in a binary reaction sequence. Surface Science 322 (1–3), 230–242.

Draper, N. R., Smith, H., 1998. Applied Regression Analysis, 3rd Edition. John Wiley & Sons, Inc., New York.

Dunham, G. C., Benson, N. H., Petelenz, D., Janata, J., 1995. Dual quartz crystal microbalance. Analytical Chemistry 67 (2), 267–272.

Edgar, T. F., Himmelblau, D. M., 1988. Optimization of Chemical Processes, 1st Edition. McGraw-Hill, New York.

Elam, J. W., George, S. M., 2003. Growth of ZnO/Al_2O_3 alloy films using atomic layer deposition techniques. Chemistry of Materials 15 (4), 1020–1028.

Elam, J. W., Groner, M. D., George, S. M., 2002. Viscous flow reactor with quartz crystal microbalance for thin film growth by atomic layer deposition. Review of Scientific Instruments 73 (8), 2981–2987.

Elam, J. W., Pellin, M. J., 2005. $GaPO_4$ sensors for gravimetric monitoring during atomic layer deposition at high temperatures. Analytical Chemistry 77 (11), 3531–3535.

Elliott, S. D., 2012. Atomic-scale simulation of ALD chemistry. Semiconductor Science and Technology 27 (7), 074008.

Fan, J.-F., Toyoda, K., 1992. Self-limiting behavior of the growth of Al_2O_3 using sequential vapor pulses of TMA and H_2O_2. Applied Surface Science 60-61, 765–769.

Ferguson, J., Weimer, A. W., George, S. M., 2000. Atomic layer deposition of ultrathin and conformal Al_2O_3 films on BN particles 371 (1–2), 95–104.

Fornberg, B., 1988. Generation of finite difference formulas on arbitrarily spaced grids. Mathematics of Computation 51 (184), 699–706.

Franceschini, G., Macchietto, S., 2008. Model-based design of experiments for parameter precision: State of the art. Chemical Engineering Science 63 (19), 4846–4872.

George, S. M., 2010. Atomic layer deposition: An overview. Chemical Reviews 110 (1), 111–131.

Granneman, E., Fischer, P., Pierreux, D., Terhorst, H., Zagwijn, P., 2007. Batch ALD: Characteristics, comparison with single wafer ALD, and examples. Surface and Coatings Technology 201 (22-23), 8899–8907.

Hangos, K. M., Cameron, I. T., 2001. Process modelling and model analysis. In: Stephanopoulos, G., Perkins, J. (Eds.), Process Systems Engineering. Vol. 4. Academic Press, London.

Henn-Lecordier, L., Anderle, M., Robertson, E., Rubloff, G. W., 2011. Impact of parasitic reactions on wafer-scale uniformity in water-based and ozone-based atomic layer deposition. Journal of Vacuum Science & Technology A 29 (5), 051509.

Hindmarsh, A. C., Brown, P. N., Grant, K. E., Lee, S. L., Serban, R., Shumaker, D. E., et al., 2005. SUNDIALS: Suite of nonlinear and differential/algebraic equation solvers. ACM Transactions on Mathematical Software 31 (3), 363–396.

Hirschfelder, J. O., Curtiss, C. F., Bird, R. B., 1964. Molecular Theory of Gases and Liquids, 2nd Edition. John Wiley & Sons, Inc., New York.

Holmqvist, A., Törndahl, T., Stenström, S., 2012. A model-based methodology for the analysis and design of atomic layer deposition processes—Part I: Mechanistic modelling of continuous flow reactors. Chemical Engineering Science 81, 260–272.

Holmqvist, A., Törndahl, T., Stenström, S., 2013a. A model-based methodology for the analysis and design of atomic layer deposition processes—Part II: Experimental validation and mechanistic analysis. Chemical Engineering Science 94, 316–329.

Holmqvist, A., Törndahl, T., Stenström, S., 2013b. A model-based methodology for the analysis and design of atomic layer deposition processes—Part III: Constrained multi-mbjective optimization. Chemical Engineering Science 96, 71–86.

Juppo, M., Rahtu, A., Ritala, M., Leskelä, M., 2000. In situ mass spectrometry study on surface reactions in atomic layer deposition of Al_2O_3 thin films from trimethylaluminum and water. Langmuir 16 (8), 4034–4039.

Jur, J. S., Parsons, G. N., 2011. Atomic layer deposition of Al_2O_3 and ZnO at atmospheric pressure in a flow tube reactor. ACS Applied Materials & Interfaces 3 (2), 299–308.

Kuse, R., Kundu, M., Yasuda, T., Miyata, N., Toriumi, A., 2003. Effect of precursor concentration in atomic layer deposition of Al_2O_3. Journal of Applied Physics 94 (10), 6411–6416.

Larrabee, T. J., Mallouk, T. E., Allara, D. L., 2013. An atomic layer deposition reactor with dose quantification for precursor adsorption and reactivity studies. Review of Scientific Instruments 84 (1), 014102.

Lei, W., Henn-Lecordier, L., Anderle, M., Rubloff, G. W., Barozzi, M., Bersani, M., 2006. Real-time observation and optimization of tungsten atomic layer deposition process cycle. Journal of Vacuum Science & Technology B 24 (2), 780–789.

Lim, J.-W., Park, J.-S., Kang, S.-W., 2000. Kinetic modeling of film growth rates of TiN films in atomic layer deposition. Journal of Applied Physics 87 (9), 4632–4634.

Lu, C.-S., Lewis, O., 1972. Investigation of film-thickness determination by oscillating quartz resonators with large mass load. Journal of Applied Physics 43 (11), 4385–4390.

Magnusson, F., Åkesson, J., Sep 2012. Collocation methods for optimization in a Modelica environment. In: 9th International Modelica Conference. Munich, Germany.

Masel, R. I., 1996. Principle of Adsorption and Reaction on Solid Surface, 1st Edition. John Wiley & Sons, Inc., New York.

Matero, R., Rahtu, A., Ritala, M., Leskelä, M., Sajavaara, T., 2000. Effect of water dose on the atomic layer deposition rate of oxide thin films. Thin Solid Films 368 (1), 1–7.

McKay, M. D., Beckman, R. J., Conover, W. J., 1979. A comparison of three methods for selecting values of input variables in the analysis of output from a computer code. Technometrics 21 (2), 239–245.

Miikkulainen, V., Leskelä, M., Ritala, M., Puurunen, R. L., 2013. Crystallinity of inorganic films grown by atomic layer deposition: Overview and general trends. Journal of Applied Physics 113 (2), 021301.

Mousa, M. B. M., Oldham, C. J., Jur, J. S., Parsons, G. N., 2012. Effect of temperature and gas velocity on growth per cycle during Al_2O_3 and ZnO atomic layer deposition at atmospheric pressure. Journal of Vacuum Science & Technology A 30 (1), 01A155.

Musgrave, C. B., 2012. Theoretical modeling of ald processes. In: Pinna, N., Knez, M. (Eds.), Atomic Layer Deposition of Nanostructured Materials, 1st Edition. Wiley-VCH Verlag GmbH & Co. KGaA, pp. 1–21.

Park, H.-S., Min, J.-S., Lim, J.-W., Kang, S.-W., 2000. Theoretical evaluation of film growth rate during atomic layer epitaxy. Applied Surface Science 158, 81–91.

Poodt, P., Cameron, D. C., Dickey, E., George, S. M., Kuznetsov, V., Parsons, G. N., et al., 2012. Spatial atomic layer deposition: A route towards further industrialization of atomic layer deposition. Journal of Vacuum Science & Technology A 30 (1), 010802.

Price, K. V., 1999. An Introduction to Differential Evolution. In: Corne, D., Dorigo, M., Glover, F. (Eds.), New Ideas in Optimization. McGraw-Hill, London, pp. 79–108.

Puurunen, R. L., 2003. Growth per cycle in atomic layer deposition: A theoretical model. Chemical Vapor Deposition 9 (5), 249–257.

Puurunen, R. L., 2004. Analysis of hydroxyl group controlled atomic layer deposition of hafnium dioxide from hafnium tetrachloride and water. Journal of Applied Physics 95 (9), 4777–4786.

Puurunen, R. L., 2005a. Correlation between the growth-per-cycle and the surface hydroxyl group concentration in the atomic layer deposition of aluminum oxide from trimethylaluminum and water. Applied Surface Science 245 (1–4), 6–10.

Puurunen, R. L., 2005b. Surface chemistry of atomic layer deposition: A case study for the trimethylaluminum/water process. Journal of Applied Physics 97 (12), 121301.

Rahtu, A., Alaranta, T., Ritala, M., 2001. In situ quartz crystal microbalance and quadrupole mass spectrometry studies of atomic layer deposition of aluminum oxide from trimethylaluminum and water. Langmuir 17 (21), 6506–6509.

Rahtu, A., Ritala, M., 2002a. Compensation of temperature effects in quartz crystal microbalance measurements. Applied Physics Letters 80 (3), 521–523.

Rahtu, A., Ritala, M., 2002b. Reaction mechanism studies on the zirconium chloride-water atomic layer deposition process. Journal of Materials Chemistry 12 (5), 1484–1489.

Reid, R. C., Prausnitz, J. M., Poling, B. E., 1988. The Properties of Gases and Liquids, 4th Edition. McGraw-Hill, New York.

Ren, J., 2009. Initial growth mechanism of atomic layer deposition of ZnO on the hydroxylated Si(100)-2×1: A density functional theory study. Applied Surface Science 255 (11), 5742–5745.

Riha, S. C., Libera, J. A., Elam, J. W., Martinson, A. B. F., 2012. Design and implementation of an integral wall-mounted quartz crystal microbalance for atomic layer deposition. Review of Scientific Instruments 83 (9), 094101.

Rimensberger, T., Rippin, D. W. T., 1986. Sequential experimental design for precise parameter estimation. 1. Use of reparameterization. Comments. Industrial & Engineering Chemistry Process Design and Development 25 (4), 1042–1044.

Ritala, M., Leskelä, M., 2002. Handbook of Thin Film Materials. Vol. 1. Academic Press, New York.

1184 Ritala, M., Niinisto, J., 2009. Industrial applications of atomic layer deposition.
1185 ECS Transactions 25 (8), 641–652.

1186 Rocklein, M. N., George, S. M., 2003. Temperature-induced apparent mass
1187 changes observed during quartz crystal microbalance measurements of atomic
1188 layer deposition. Analytical Chemistry 75 (19), 4975–4982.

1189 Sauerbrey, G., 1959. Verwendung von schwingquarzen zur wägung dünner
1190 schichten und zur mikrowägung. Zeitschrift für Physik A Hadrons and Nuclei
1191 155, 206–222.

1192 Schiesser, W. E., 1991. The Numerical Method of Lines: Integration of Partial
1193 Differential Equations, 1st Edition. Academic Press, San Diago.

1194 Schwaab, M., Lemos, L. P., Pinto, J. C., 2008. Optimum reference temperature
1195 for reparameterization of the Arrhenius equation. Part 2: Problems involving
1196 multiple reparameterizations. Chemical Engineering Science 63 (11), 2895–
1197 2906.

1198 Schwaab, M., Pinto, J. C., 2007. Optimum reference temperature for reparam-
1199 eterization of the Arrhenius equation. Part 1: Problems involving one kinetic
1200 constant. Chemical Engineering Science 62 (10), 2750–2764.

1201 Schwaab, M., Pinto, J. C., 2008. Optimum reparameterization of power function
1202 models. Chemical Engineering Science 63 (18), 4631–4635.

1203 Semiconductor Industry Association, 2011. Modeling and simula-
1204 tions. In: The International Technology Roadmap for Semiconduc-
1205 tors, 2011th Edition. San Jose, CA, pp. 1–45, [Online]. Avaliable:
1206 `http://public.itrs.net/reports.html`.

1207 Sneh, O., Clark-Phelps, R. B., Londergan, A. R., Winkler, J., Seidel, T. E., 2002.
1208 Thin film atomic layer deposition equipment for semiconductor processing.
1209 Thin Solid Films 402 (1-2), 248–261.

Storn, R., Price, K., 1997. Differential Evolution - A simple and efficient heuristic for global optimization over continuous spaces. Journal of Global Optimization 11 (4), 341–359.

Suntola, T., 1992. Atomic layer epitaxy. Thin Solid Films 216 (1), 84–89.

The Modelica Association, 2012. The Modelica Association Home Page. `http://www.modelica.org`.

Törndahl, T., Platzer-Björkman, C., Kessler, J., Edoff, M., 2007. Atomic layer deposition of $Zn_{1-x}Mg_xO$ buffer layers for $Cu(In,Ga)Se_2$ solar cells. Progress in Photovoltaics: Research and Applications 15 (3), 225–235.

Travis, C. D., Adomaitis, R. A., 2013a. Dynamic modeling for the design and cyclic operation of an atomic layer deposition (ALD) reactor. Processes 1 (2), 128–152.

Travis, C. D., Adomaitis, R. A., 2013b. Modeling ALD surface reaction and process dynamics using absolute reaction rate theory. Chemical Vapor Deposition 19, 1–11.

Vegliò, F., Trifoni, M., Pagnanelli, F., Toro, L., 2001. Shrinking core model with variable activation energy: A kinetic model of manganiferous ore leaching with sulphuric acid and lactose. Hydrometallurgy 60 (2), 167–179.

Wächter, A., Biegler, L. T., 2006. On the implementation of an interior-point filter line-search algorithm for large-scale nonlinear programming. Mathematical Programming 106 (1), 25–57.

Wajid, A., 1991. Improving the accuracy of a quartz crystal microbalance with automatic determination of acoustic impedance ratio. Review of Scientific Instruments 62 (8), 2026–2033.

Watts, D. G., 1994. Estimating parameters in nonlinear rate equations. Canadian Journal of Chemical Engineering 72 (4), 701–710.

Widjaja, Y., Musgrave, C. B., 2002a. Atomic layer deposition of hafnium oxide: A detailed reaction mechanism from first principles. The Journal of Chemical Physics 117 (5), 1931–1934.

Widjaja, Y., Musgrave, C. B., 2002b. Quantum chemical study of the elementary reactions in zirconium oxide atomic layer deposition. Applied Physics Letters 81 (2), 304–306.

Wilke, C. R., 1950. A viscosity equation for gas mixtures. Journal of Chemical Physics 18 (4), 517–519.

Wind, R. A., George, S. M., 2010. Quartz Crystal Microbalance Studies of Al_2O_3 Atomic Layer Deposition Using Trimethylaluminum and Water at 125 °C. The Journal of Physical Chemistry A 114 (3), 1281–1289.

Wolden, C. A., Kurtin, J., Baxter, J. B., Repins, I., Shaheen, S. E., Torvik, J. T., et al., 2011. Photovoltaic manufacturing: Present status, future prospects, and research needs. Journal of Vacuum Science & Technology A 29 (3), 030801.

Yanguas-Gil, A., Elam, J. W., 2012. Simple model for atomic layer deposition precursor reaction and transport in a viscous-flow tubular reactor. Journal of Vacuum Science & Technology A 30 (1), 01A159.

Ylilammi, M., 1995. Mass transport in atomic layer deposition carrier gas reactors. Journal of The Electrochemical Society 142 (7), 2474–2479.

Yousfi, E. B., Fouache, J., Lincot, D., 2000. Study of atomic layer epitaxy of zinc oxide by in-situ quartz crystal microgravimetry. Applied Surface Science 153 (4), 223–234.